BioMed Research International

Mesenchymal Stem Cell Therapy in Regenerative Medicine: Latest Developments and Trends

Lead Guest Editor: Alok Raghav
Guest Editors: Yanbo Zhang and Jia Xian Law

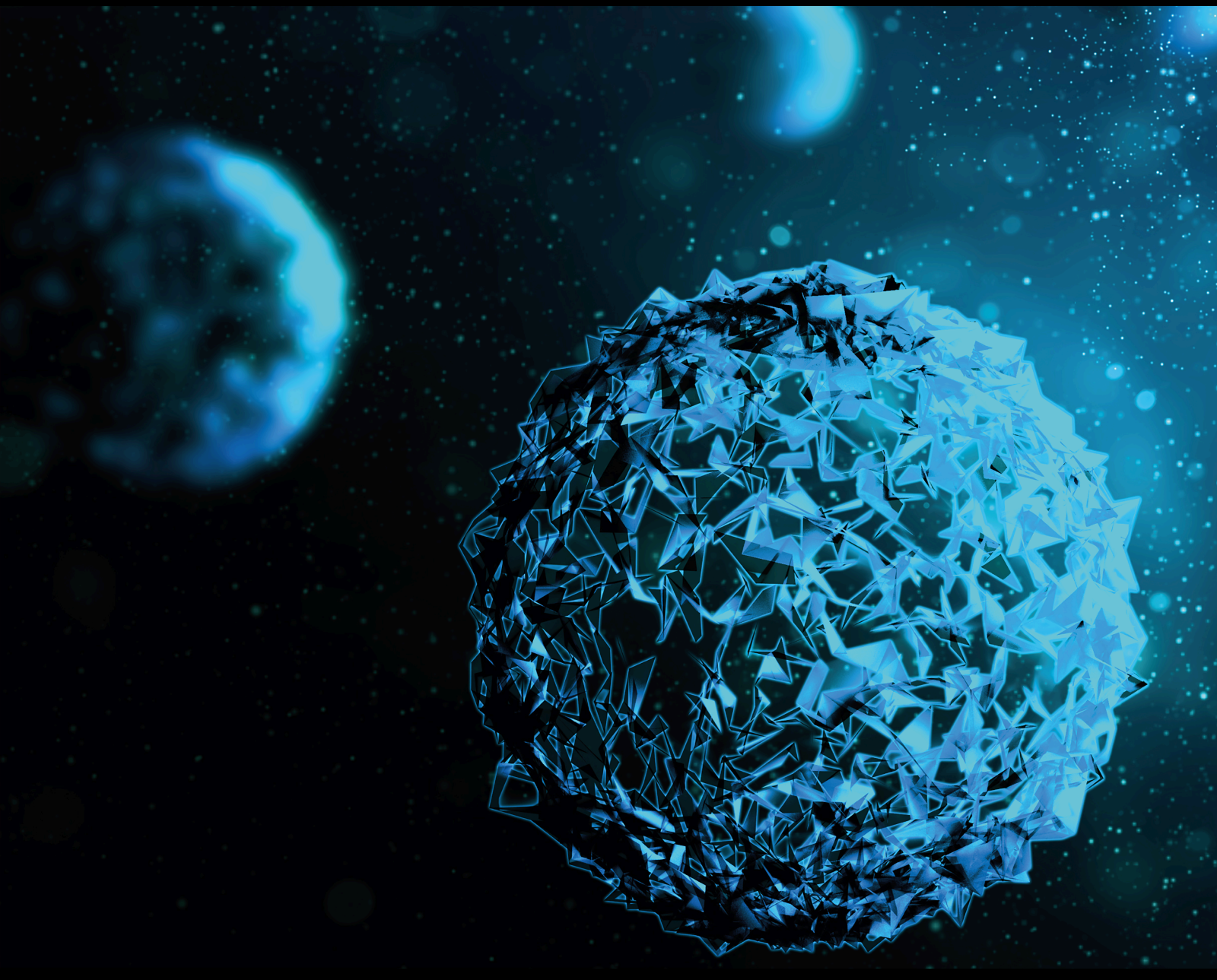

Mesenchymal Stem Cell Therapy in Regenerative Medicine: Latest Developments and Trends

BioMed Research International

Mesenchymal Stem Cell Therapy in Regenerative Medicine: Latest Developments and Trends

Lead Guest Editor: Alok Raghav
Guest Editors: Yanbo Zhang and Jia Xian Law

Section Editors

Penny A. Asbell, USA
David Bernardo, Spain
Gerald Brandacher, USA
Kim Bridle, Australia
Laura Chronopoulou, Italy
Gerald A. Colvin, USA
Aaron S. Dumont, USA
Pierfrancesco Franco, Italy
Raj P. Kandpal, USA
Fabrizio Montecucco, Italy
Mangesh S. Pednekar, India
Letterio S. Politi, USA
Jinsong Ren, China
William B. Rodgers, USA
Harry W. Schroeder, USA
Andrea Scribante, Italy
Germán Vicente-Rodriguez, Spain
Momiao Xiong, USA
Hui Zhang, China

Academic Editors

Pathology

Atif A. Ahmed, USA
Shinichi Aishima, Japan
Valeria Barresi, Italy
Ewa Bien, Poland
Tarek A. Bismar, Canada
Rosario Caltabiano, Italy
Jin-Jer Chen, China
Chandu De Silva, Sri Lanka
Vasiliki Galani, Greece
Wan-Ming Hu, China
Genichiro Ishii, Japan
Glen Jickling, USA
Shigeru Kobayashi, Japan
Kun Li, China
Satoshi Maruyama, Japan
Kathleen Montone, USA
Yukihiro Nakanishi, USA
Stefania Pizzimenti, Italy
Jianyu Y. Rao, USA
Takashi Saku, Japan
Claire Troakes, United Kingdom
Koichiro Wada, Japan

Contents

Hindawi
BioMed Research International
Volume 2023, Article ID 9765196, 1 page
https://doi.org/10.1155/2023/9765196

Retraction

Retracted: Gastrocnemius Muscle Injury Is the Condition to Induce Cartilage Degeneration of the Rabbit Tibiofemoral Joint: A New Perspective

BioMed Research International

Received 26 September 2023; Accepted 26 September 2023; Published 27 September 2023

This article has been retracted by Hindawi following an investigation undertaken by the publisher [1]. This investigation has uncovered evidence of one or more of the following indicators of systematic manipulation of the publication process:

(1) Discrepancies in scope

(2) Discrepancies in the description of the research reported

(3) Discrepancies between the availability of data and the research described

(4) Inappropriate citations

(5) Incoherent, meaningless and/or irrelevant content included in the article

(6) Peer-review manipulation

The presence of these indicators undermines our confidence in the integrity of the article's content and we cannot, therefore, vouch for its reliability. Please note that this notice is intended solely to alert readers that the content of this article is unreliable. We have not investigated whether authors were aware of or involved in the systematic manipulation of the publication process.

In addition, our investigation has also shown that one or more of the following human-subject reporting requirements has not been met in this article: ethical approval by an Institutional Review Board (IRB) committee or equivalent, patient/participant consent to participate, and/or agreement to publish patient/participant details (where relevant).

Wiley and Hindawi regrets that the usual quality checks did not identify these issues before publication and have since put additional measures in place to safeguard research integrity.

We wish to credit our own Research Integrity and Research Publishing teams and anonymous and named external researchers and research integrity experts for contributing to this investigation.

The corresponding author, as the representative of all authors, has been given the opportunity to register their agreement or disagreement to this retraction. We have kept a record of any response received.

References

[1] Y. Li, J. Sun, Y. Hou et al., "Gastrocnemius Muscle Injury Is the Condition to Induce Cartilage Degeneration of the Rabbit Tibiofemoral Joint: A New Perspective," *BioMed Research International*, vol. 2022, Article ID 7532434, 12 pages, 2022.

Hindawi
BioMed Research International
Volume 2022, Article ID 2475169, 15 pages
https://doi.org/10.1155/2022/2475169

Research Article

HIF1α Promotes BMP9-Mediated Osteoblastic Differentiation and Vascularization by Interacting with CBFA1

Yuwan Li,[1] **Ziming Liu**,[1] **Hong-De Wang**,[1] **Jun Zhang**,[2] **Miaoyuan Lin**,[3] **Jianye Yang**,[2] **Jiaxing Huang**,[2] **Wenqiang Yan**,[1] **and Yingfang Ao**[1]

[1]*Department of Sports Medicine, Peking University Third Hospital, Institute of Sports Medicine of Peking University, Beijing Key Laboratory of Sports Injuries, Beijing 100191, China*
[2]*Department of Orthopaedics, The First Affiliated Hospital of Chongqing Medical University, Chongqing 400016, China*
[3]*Department of Orthopaedics, The First Affiliated Hospital of Zunyi Medical University, Zunyi, 563000 Guizhou, China*

Correspondence should be addressed to Yingfang Ao; aoyingfang@163.com

Received 27 June 2022; Accepted 26 August 2022; Published 1 October 2022

Academic Editor: Alok Raghav

Bone morphogenetic protein 9 (BMP9) as the most potent osteogenic molecule which initiates the differentiation of stem cells into the osteoblast lineage and regulates angiogenesis, remains unclear how BMP9-regulated angiogenic signaling is coupled to the osteogenic pathway. Hypoxia-inducible factor 1α (HIF1α) is critical for vascularization and osteogenic differentiation and the CBFA1, known as runt-related transcription factor 2 (Runx2) which plays a regulatory role in osteogenesis. This study investigated the combined effect of HIF1α and Runx2 on BMP9-induced osteogenic and angiogenic differentiation of the immortalized mouse embryonic fibroblasts (iMEFs). The effect of HIF1α and Runx2 on the osteogenic and angiogenic differentiation of iMEFs was evaluated. The relationship between HIF1α- and Runx2-mediated angiogenesis during BMP9-regulated osteogenic differentiation of iMEFs was evaluated by ChIP assays. We demonstrated that exogenous expression of HIF1α and Runx2 is coupled to potentiate BMP9-induced osteogenic and angiogenic differentiation both *in vitro* and animal model. Chromatin immunoprecipitation assays (ChIP) showed that Runx2 is a downstream target of HIF1α that regulates BMP9-mediated osteogenesis and angiogenic differentiation. Our findings reveal that HIF1α immediately regulates Runx2 and may originate an essential regulatory thread to harmonize osteogenic and angiogenic differentiation in iMEFs, and this coupling between HIF1α and Runx2 is essential for bone healing.

1. Introduction

Mesenchymal progenitor cells (MPCs) exhibit self-renewal capacity and rapidly proliferate and differentiate into multiple lineages including osteogenic, chondrogenic, myogenic, and adipogenic cell lines [1–4]. Mouse embryonic fibroblasts (MEFs) are mesenchymal stem cells that could be able to undergo multidirectional differentiation potential which is into osteogenic, chondrogenic, and angiogenic cell lines [5]. Immortalized mouse embryonic fibroblasts (iMEFs) could be capable of conditionally immortalized MEFs that possess increased proliferative ability and long-term maintenance of cell proliferation [6]. iMEFs can be induced to undergo phenotype reversal by Cre recombinase, in possession of most markers of MPCs and retain multiple directional differentiation potential, as they can differentiate into osteogenic and angiogenic lineages under suitable conditions [7, 8]. iMEFs can be used in regenerative medicine as effective seed cells to treat bone defects, nonunion, and osteogenic-related diseases due to their proliferation and differentiation abilities and stromal progenitor cell biology [9].

Osteogenic differentiation is a continuous cascade that recaps nearly entire of the molecular adjustments that occur throughout embryonic skeletal development [10]. Bone morphogenetic proteins (BMPs) consist of nearly 20 members that be part of the transforming growth factor beta (TGF-β) superfamily [11]. Recombinant human bone morphogenic proteins, including BMP4 and BMP7, have been extensively used in clinical applications for the efficient stimulation of bone formation and for treating bone defects [12].

It has been reported that BMP9 can be used for filling engineered bone and treating osseous defects. When combined with some biomaterials, the release of the growth factor can be controlled at the proper rate. BMP9 as one of the most potent BMPs, can induce osteogenic differentiation of multipotent progenitor cells [13]. The effect of BMP9-induced osteoblast differentiation is enhanced by regulating several downstream targets, such as HIF1α [14], Runx2 [15], Hey1 [16], and COX-2 [17]. However, the connotative mechanism involved in BMP9 mediated osteogenesis was still unclear.

Hypoxia-inducible factor 1α (HIF1α) is a generally accepted angiogenesis cascade regulator that is involved in many biological and organic developmental processes, including tumor-related and skeletal development. Some studies also indicated that HIF1α helps promote BMP9-induced angiogenic and osteogenic differentiation though BMP/Smad signaling in iMEFs. Runx2 is a specific transcription factor in mature bone cells that plays an important role in the formation and reconstruction of bone tissue. Runx2 regulates the differentiation of iMEFs into osteoblasts and promotes the maturation and vascularization of cartilage. Additionally, this protein is involved in the synthesis of extracellular matrix. However, it is currently unclear whether and how the angiogenic factor HIF1α is coupled with the osteogenic factor Runx2 during BMP9-induced osteogenesis in iMEFs. It is also ambiguous whether these factors mutually participate in this regulation.

In this study, we investigated the role of HIF1α and Runx2 on BMP9-induced angiogenic and osteogenic differentiation in MEFs. We found that exogenous overexpression of HIF1α and Runx2 intensifies BMP9-induced osteogenic and angiogenic differentiation of iMEFs *in vitro* and in animal model, whereas RNA-mediated silencing of HIF1α and Runx2 strongly dulls BMP9-induced angiogenic and osteogenic signaling in iMEFs. Mechanistically, HIF1α can directly regulate Runx2 expression at the transcript and protein levels. Our findings no mere broad our understanding of the molecular events underlying BMP9-induced osteoblast-specific differentiation but also suggest that targeting the coupling of BMP9-induced angiogenic and osteogenic signaling may become a new approach for vascular-targeted therapy in bone tissue engineering.

2. Materials and Methods

2.1. Cell Culture and Chemicals. The experiment was approved by the Ethics Committee of the First Affiliated Hospital of Chongqing Medical University, and the written informed consent was obtained before surgery. HEK-293 cells and iMEFs were obtained from ATCC (Manassas, VA, USA). Cells were maintained in low-glucose Dulbecco's modified Eagle's medium (LG-DMEM) containing 10% fetal bovine serum (FBS), 100 U/mL penicillin, and 100 mg/mL streptomycin. The cells were incubated at 37°C with 5% CO_2. The cultured medium was changed every three to four days.

2.2. Recombinant Adenovirus Arrangement. The recombinant adenoviruses were constructed with AdEasy technology [18, 19]. To be short, the core regions of genes encoding BMP9, HIF1α, green fluorescent protein (GFP), red fluorescent protein (RFP), and Runx2 were amplified by quantitative real-time reverse transcription polymerase chain reaction (qRT–PCR), cloned into shuttle vectors which could be subjected to amplify recombinant adenoviruses in HEK-293 cells. The target sites of siRNA against mouse HIF1α and Runx2 coding regions were amplified into the pSES adenoviral shuttle vector which form recombinant adenoviruses. The adenoviruses nominated Ad-BMP9, Ad-HIF1α, Ad-Runx2, Ad-Sim-HIF1α, and Ad-Sim-Runx2. Ad-BMP9 expressed GFP, while Ad-HIF1α, Ad-Sim-HIF1α, Ad-Runx2, and Ad-Sim-Runx2 expressed RFP as a visual sign for observing efficiency of infection. Analogous adenoviruses expressing monomeric GFP (Ad-GFP) served as negative controls.

2.3. Gene Expression of Osteogenesis- and Angiogenesis-Related mRNA. The cells were cultured according to the experimental design. Total RNA was gained with TRIzol reaction agentia, and cDNA was extracted from RNA with a reverse transcription reaction reagent (RR047A, TAKARA, Japan). The first-strand cDNA products were diluted 5-10-fold and used as templates for detection by real-time qRT-PCR (RR820A, TAKARA). The amplification conditions were set: predenaturation, denaturation, and annealing. GAPDH served as the internal control set. Expression levels of target genes from various groups were measured using the $2^{\Delta\Delta CT}$ method. Gene expression of collected samples was conducted triplicate. The information of primers for PCR are shown in Table 1.

2.4. Chromatin Immunoprecipitation (ChIP) Assay. Subconfluent iMEFs were treated with infection of Ad-GFP or Ad-BMP9 and Ad-HIF1α. The cell samples were cross-linked after 48 hours of infection, then subjected to ChIP analysis according to the manufacturer's instructions (#9003, CST). The cells were incubated with a rabbit anti-mouse HIF1α (HIF1α67, Abcam) antibody or IgG to pull down the DNA-protein Mmixture. The Runx2 promoter sequence was determined using four pairs of primers consistent with the mouse Runx2 sites. The relevant primers and sequences of promoter information of the ChIP assay are listed in Supplementary Tables 1 and 2.

2.5. Alkaline Phosphatase (ALP) Expression Assay. ALP expression was measured by a modified automated chemiluminescence assay (BD Company, USA) and histochemical staining, according to the manufacturers' instruction [20, 21]. Cells were treated with infection of Ad-GFP, Ad-HIF1α, Ad-BMP9, Ad-Runx2, and Ad-BMP9 combined with Ad-HIF1α, Ad-BMP9 combined with Ad-Runx2, Ad-BMP9 combined with Ad-SimHIF1α, or Ad-BMP9 combined with Ad-Sim-Runx2. In the chemiluminescence detection and quantification test, each sample was tested for three times, and the tests were repeated in at least three independent experiments. In addition, ALP expression was standardized

Table 1: Primer sequence of the target genes.

Gene	Forward primer (5′-3′)	Reverse primer (5′-3′)	Product length
BMP9	TACAACAGATACACAACGGACA	GATGTTGAAGATCAGGATGTGC	135
Runx2	CAGACCAGCAGCACTCCATATC	CCGTCAGCGTCAACACCATC	182
HIF1α	TGCTCATCAGTTGCCACTTCC	TGCCTTCATCTCATCTTCACTGTC	139
OPN	GACCGTCACTGCTAGTACACAAG	CCTTAGACTCACCGCTCTTCATG	194
BSP	AAGCACAGACTTTTGAGTTAGC	ACTTCTGCTTCTTCGTTCTCAT	145
COL-A1	TGAACGTGGTGTACAAGGTC	CCATCTTTACCAGGAGAACCAT	234
VEGF	CACGACAGAAGGAGAGCAGAAG	CTCAATCGGACGGCAGTAGC	82
ANGPT1	TTCTTCGCTGCCATTCTGACTCAC	GTTGTACTGCTCTGTCGCACTCTC	165
vWF	ACAGTAACATGGAGATGGCAGTG	TTGTGGCGTGTATGTGAGGATG	143

to the total cellular protein level of cell samples. ALP expression was presented as the mean ± standard deviation.

2.6. Matrix Mineralization Detection. iMEFs were inoculated in 24-well plates for 6 h seeded at a density of 30% and then infected with Ad-BMP9, Ad-HIF1α, or Ad-Runx2. The osteoblastic differentiation-conditioned medium contained ascorbic acid and β-phosphoglycerol for 21 days. The matrix mineralization activity was evaluated by Alizarin Red S staining. The cell samples were soaked with 2.5% glutaraldehyde 15 min at room temperature, washed with PBS solution for three times. The mineralized tubercles were stained with 0.4% (v/v) Alizarin Red S dyestuff for 10 min, then washed with double distilled water for 15 min. Mineralization was observed under a microscope, and at least 3 independent experiments were conducted.

2.7. Nano-Glo Dual-Luciferase Reporter Assay. The iMEFs were seeded in Corning 24-well cell culture plates and transfected with 1 μg firefly luciferase vector, 1 μg Renilla luciferase vector, and 0.5 μg BMP9 binding element luciferase reporter (p12Xsbe-Luc) or Runx2 reporter plasmid (p6Xose2-Luc) per flask using Lipofectamine 2000 [22, 23]. Twenty-four hours after transfection, the cells were reseeded in 24-well plates and treated with DMSO, HIF1α, and/or Runx2. After 36 h, the cell samples were lysed and subjected to a luciferase assay using a Promega Luciferase assay kit (E1500; Promega, Madison, WI, USA). Luciferase activities were normalized by detecting the concentration of total cellular protein.

2.8. Immunohistochemical Staining. Cells were infected with adenovirus and treated in accordance with the experimental design. The iMEFs were seeded onto sterile sections in 12-well plates at a density of 10^4 cells/mL. The cells were washed 3 times with PBS for 10 min, then the cells were fixed with 4% paraformaldehyde at 37°C for 15 min, washed 3 times with PBS for 10 min, and permeabilized using 0.3% Triton X-100 for 30 minutes at 37°C. The cell samples were blocked with goat serum for 30 minutes after permeabilization. The samples were then incubated with primary antibodies overnight. The results of the expected protein were visualized by incubation with the appropriate fluorescently labeled secondary antibody. The sections were carefully removed and then mounted on slides with glycerol.

2.9. Stem Cell Implantation and Ectopic Ossification. iMEFs were transfected with appointed adenoviruses and prepared for injection at 5×10^6 cells into the side abdomen of athymic nude mice (4-7-week-old male, Sprague–Dawley) until fluorescence could be seen. Five weeks after injection, the mice were euthanized, and bony masses were obtained for micro-CT imaging and histologic staining and evaluation.

2.10. Microcomputed Tomographic Imaging Analysis. The bone masses were retrieved and scanned with SkyScan1174 X-ray microtomography (micro-CT) (Bruker Company, Belgium) after the animals were euthanized at 5 weeks. The 3D image reconstruction was analyzed with N-Recon software, and all image data analysis was performed using CT-SCAN software. Histomorphological parameters of bone formation including bone volume/total volume (BV/TV), trabecular number (Tb.N), trabecular separation (Tb.Sp), trabecular thickness (Tb.Th), and bone mineral density were detected.

2.11. Hematoxylin and Eosin (H&E) and Trichrome Staining. The bone mass samples were collected and decalcified with 10% EDTA solution, then soaked in PBS for three times and fixed in 4% paraformaldehyde. The samples embedded in paraffin were subjected to H&E and Trichrome Masson's staining in accordance with manufacturers' instructions [24, 25].

2.12. HUVEC Tube Formation Assay. HUVECs were seeded in the enhanced endothelial conditioned medium (ECM), which is containing 10% FBS, 2 mM L-glutamine, 100 U/mL penicillin, 100 μg/mL streptomycin, and 1% ECGS (Sigma, USA) for 4 h. The HUVECs were transferred into lower storey of the Transwell which is the preparation of Matrigel at a density of 10^5 cells per well. Then, the experimental iMEFs transfected with adenovirus were transferred into the upper wells. The Transwell was incubated at 37°C for 4 h. The tube area was quantified with the relative area of tube structures formed. The relative area of tubes was counted for three times per well and averaged from three images per well using Image J software (National Institutes of Health, USA).

2.13. Subcutaneous PLGA-iMEF Hybrid Implantation to Detect Angiogenesis. iMEFs were transfected with specific adenovirus in accordance with the study design for 24 h and transferred onto poly (lactic-co-glycolic acid) (PLGA) scaffolds. Eighteen mice (6-week-old males; BALB/cAnN, Chongqing, China) weighing 18-25 g were anesthetized with 1% pentobarbital sodium (30 mg/kg), and then, PLGA scaffolds carrying transfected iMEFs were implanted into the subcutaneous region of nude mice. At the end of the fifth week, the implants were harvested. The PLGA-iMEF composites were collected and analyzed after 5 weeks. The PLGA scaffold-iMEF composites were retrieved. The samples were, respectively, decalcified and paraffin-embedded, then the sections were performed with immunohistochemical staining for CD31 (Abcam, USA), then incubated with the fluorophore-conjugated antibodies.

2.14. Statistical Analysis. The results were assessed; the data represented correspond to the mean ± SD if not stated. Experiment was conducted three times $n = 3$. Statistical analyses were performed using GraphPad Prism app (CA, USA). Student-Newman-Keuls T tests and one-way ANOVA were used to analyze the significant differences from various groups. Level of significance was determined as $p < 0.05$ significance.

3. Results

3.1. HIF1α and Runx2 Promote BMP9-Mediated Osteoblastic Differentiation of iMEFs. To determine whether HIF1α and Runx2 are critical targets of BMP9-mediated osteogenic and angiogenic signaling, we sought to explore whether exogenous expression of HIF1α and Runx2 participates in BMP9-induced osteogenic differentiation of iMEFs. Recombinant adenoviruses expressing HIF1α (Ad-HIF1α) or Runx2 (Ad-Runx2) were constructed. The results demonstrated that HIF1α and Runx2 effectively mediate transgene expression in iMEFs (Supplementary Figure 1A). Alkaline phosphatase (ALP), an indicator of early-stage osteogenic differentiation, was used to detect ALP activity. The results qualitatively and quantitatively showed that HIF1α and Runx2 exerted an intense synergistic effect on BMP9-induced ALP activity. On day 7, HIF1α and Runx2 significantly enhanced BMP9-mediated ALP expression, while exogenous HIF1α and Runx2 alone did not produce a marked effect on the early stage of osteogenic differentiation (Figures 1(a) and 1(c)). The calcium deposition and mineralization levels of iMEFs in the BMP9+HIF1α and BMP9+ Runx2 groups were higher than those in the HIF1α, Runx2, and GFP groups on day 21 (Figures 1(b) and 1(c)). Bone sialoprotein (BSP), collagen type I (COL-A1), and osteopontin (OPN) are essential indicators of osteogenic differentiation of iMEFs. To further confirm whether HIF1α and Runx2 are vital mediators of BMP9-mediated osteogenesis, we investigated the role of HIF1α and Runx2 on the mRNA expression of genes encoding BSP, COL-A1, and OPN. The results demonstrated that the mRNA expression levels of genes encoding BSP, COL-A1, and OPN in the BMP9+HIF1α group were significantly upregulated compared with the levels in the BMP9 group and the HIF1α group at day 7. Consistent with the Runx2-mediated effect on osteogenic differentiation, the mRNA levels of these factors in the BMP9+Runx2 group were greatly increased compared to the levels in the GFP and Runx2 groups on day 7 (Figure 2(a)). Remarkably, the expression of genes encoding BSP, COL-A1, and OPN was also lower in the HIF1α and Runx2 groups than in the GFP group. Taken together, these results strongly indicated that HIF1α and Runx2 can critically potentiate the BMP9-induced early and late osteoblastic differentiation of iMEFs *in vitro*.

3.2. Silencing HIF1α and Runx2 Inhibits BMP9-Mediated Osteogenesis. We further confirmed that HIF1α and Runx2 are essential mediators of BMP9-induced osteogenic signaling. We used recombinant adenovirus expressing a pool of three siRNAs poniting the coding regions of mouse HIF1α and Runx2 using pSOS system, generating Ad-Sim-HIF1α and Ad-Sim-Runx2. On day 7, the results showed that compared with that of the Sim-Runx2 group, ALP activity was greatly decreased in iMEFs after transfection with Ad-Sim-HIF1α. Qualitatively, ALP staining results presented similar results, and the expression of Sim-HIF1α drastically reduced ALP activity in iMEFs induced by BMP9 (Figures 3(a) and 3(c)). Moreover, Sim-HIF1α expression almost totally blunted BMP9-mediated bone mineralization in iMEFs, as shown by Alizarin Red S staining and the relative mineralization rate on day 21 (Figures 3(b) and 3(c)). Similarly, the qRT–PCR results illustrated that the expression of genes encoding osteogenesis-related factors such as BSP, COL-A1, and OPN was significantly downregulated in the Sim-HIF1α group compared to the BMP9 group at day 7 (Figure 2(a)). In short, these results strongly demonstrated that silencing HIF1α and Runx2 expression may exert a negative regulatory effect on the BMP9-induced osteogenic differentiation of iMEFs.

3.3. HIF1α and Runx2 Are Critical for Junctional Differentiation of BMP9-Induced Subcutaneous Bone Formation in Nude Mice. It still remains unknown whether HIF1α and Runx2 could affect bone formation *in vivo*. We hence utilized a subcutaneous bone formation model to detect the effects of HIF1α and/or Runx2 on BMP9-induced ossification. The general morphology and micro-CT three-dimensional (3D) reconstruction results demonstrated that the general sizes of bony masses from the BMP9+HIF1α group were larger than those of bony masses from all other groups. The volume of osteogenic masses was smaller in the BMP9+Runx2 group than that in the BMP9 +HIF1α group, while the BMP9+Sim-HIF1α group showed a distinct decrease compared with the BMP9+Sim-Runx2 group (Figure 4(a)). The average mineral density displayed by the heatmap analysis revealed that HIF1α and Runx2 expression potentiated the average mineralization formed by BMP9-induced iMEFs. Notably, silencing exogenic HIF1α and Runx2 expression robustly decreased the average mineral density, but the effect of silencing HIF1α was greater than the effect of silencing Runx2 (Figure 4(c)). Quantitative results of bone parameters showed that the values including bone volume/total volume (BV/TV), trabecular number (Tb.N), trabecular thickness (Tb.Th), and bone mineral

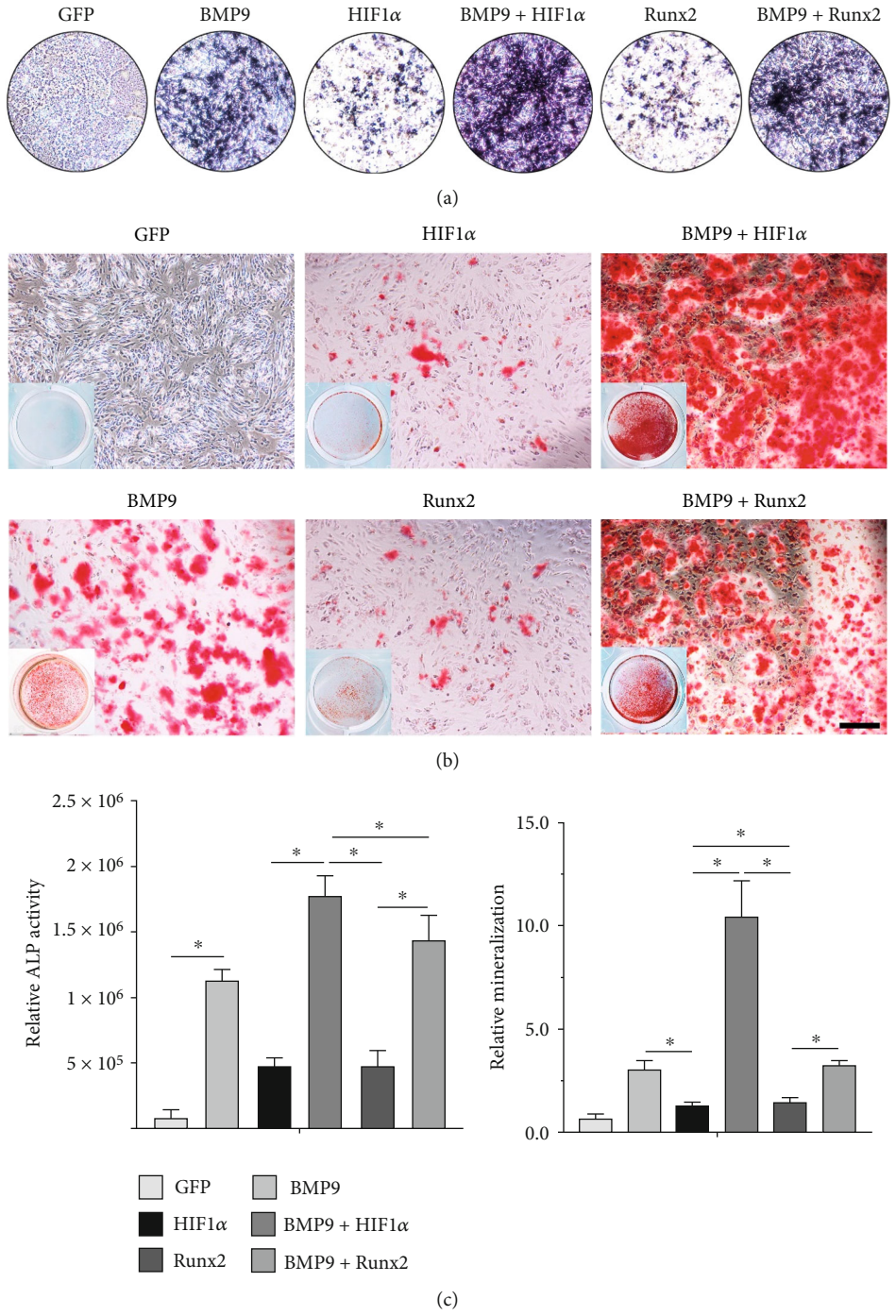

Figure 1: HIF1α and Runx2 potentiate BMP9-induced early osteogenic differentiation and late matrix mineralization of iMEFs. (a) Overexpression of HIF1α promotes BMP9-induced alkaline phosphatase (ALP) activity in iMEFs. (b) An Alizarin Red S staining assay was used to evaluate the matrix mineralization of iMEFs. Representative gross images and microscopic images in response to the above treatments are shown after transfection. Alizarin Red S staining shows the effect of HIF1α and Runx2 on BMP9-induced matrix mineralization in iMEFs (scale bar = 100 μm). (c) Quantification results showed that HIF1α and Runx2 enhanced BMP9-induced ALP activity and matrix mineralization, respectively ($^*p < 0.05$).

density (BMD) were significantly higher in the BMP9 +HIF1α group than in the other groups. However, the values of these parameters in the BMP9+Sim-Runx2 group were significantly higher than those in the BMP9+ Sim-HIF1α group. There were no significant differences in trabecular spacing (Tb.Sp) among groups (Figure 4(b)).

The retrieved bone blocks were further subjected to histologic staining. The H&E and Masson's trichrome staining results demonstrated that compared with the BMP9 group, overexpression of HIF1α and Runx2 significantly promoted the number and quality of trabecular bone as well as mineralization, and HIF1α increased these values more than

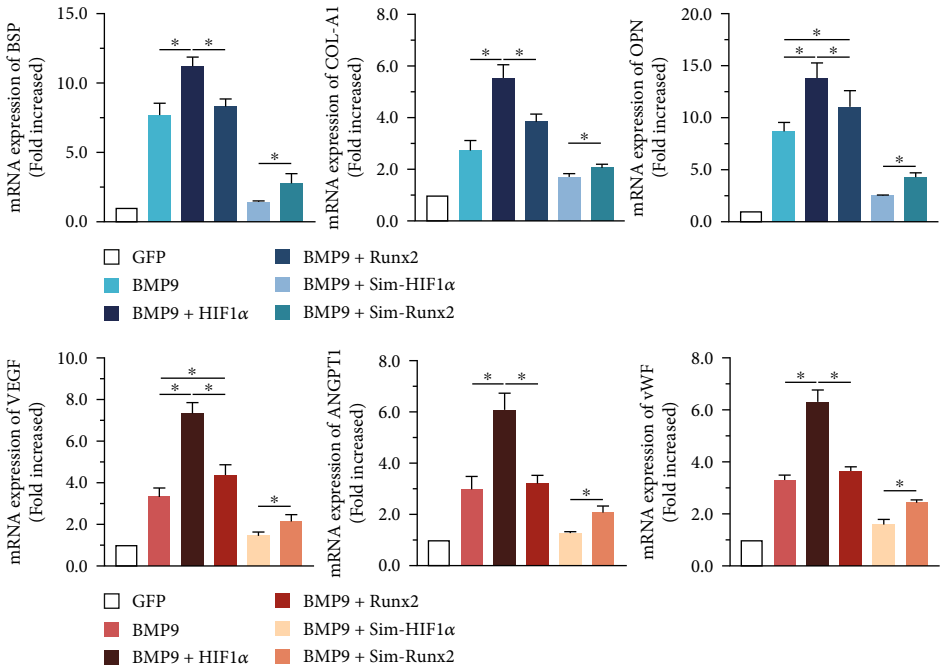

(a)

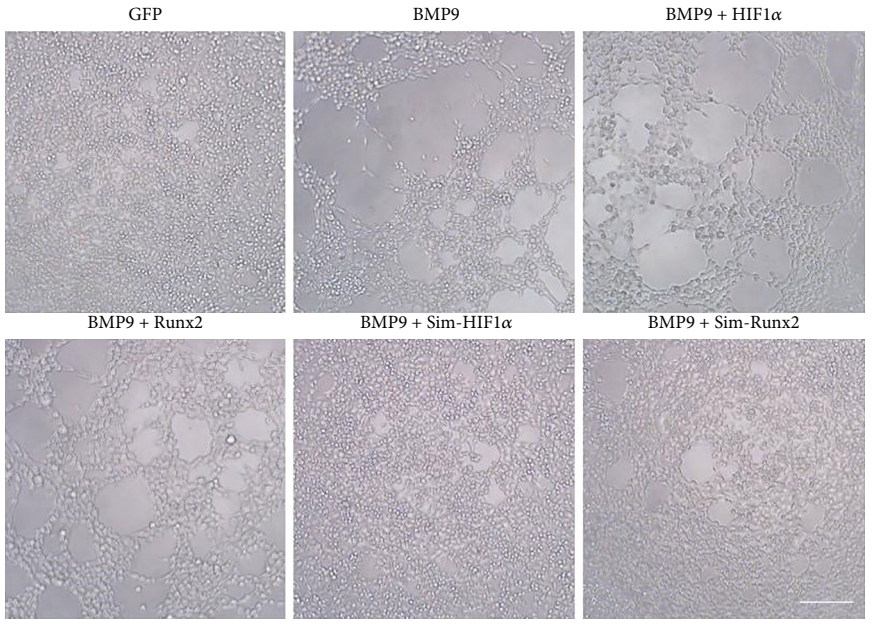

(b)

Figure 2: Continued.

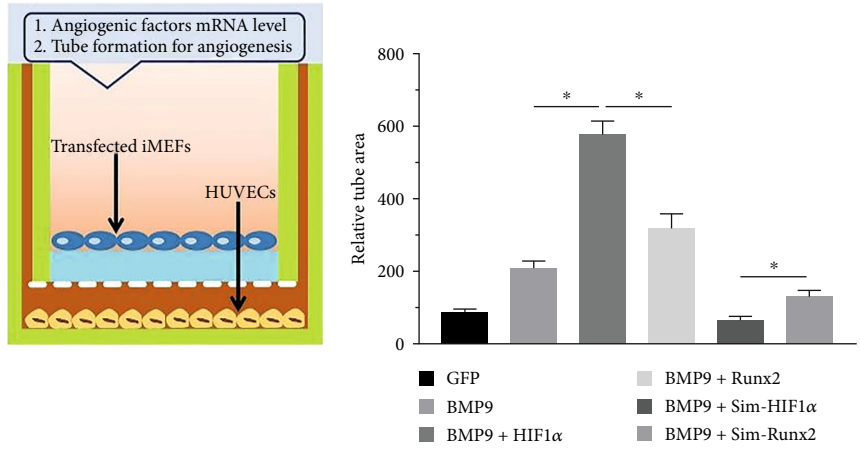

Figure 2: Effects of HIF1α and Runx2 on BMP9-induced early osteogenic and angiogenic differentiation in iMEFs. (a) Effect of mRNA expression of HIF1α and Runx2 on BMP9-induced osteogenic and angiogenic regulators, including VEGF, ANGPT1, and vWF, on day 7 ($^*p < 0.05$). (b) Microscopy images of the effect of transfected iMEFs on tube formation by HUVECs (scale bar = 100 μm). (c) Experimental design for the assay investigating the early effects on HUVEC tube formation. HUVECs were incubated in ECM medium for 12 h and plated on a Matrigel layer. iMEFs transfected with adenovirus were seeded into the upper wells. Tube formation was recorded over the course of 6 h. (d) Quantification of tube formation by HUVECs. The relative tube area was quantified to measure tube formation, and all values are shown for each group ($^*p < 0.05$).

Runx2 (blue in Masson's trichrome and red in H&E) among groups. Moreover, silencing HIF1α and Runx2 significantly decreased the amount of trabecular bone. Notably, less trabecular bone and bone matrix formation was observed in the BMP9+Sim-HIF1α group than in the BMP9+Sim-Runx2 group (Figure 4(d)).

3.4. HIF1α and Runx2 Regulate Angiogenic Differentiation and Vasoformation during BMP9-Mediated Osteogenesis. To further confirm the potential of angiogenic differentiation and vasoformation regulated by HIF1α and Runx2, we used qRT–PCR of the transfected iMEFs on day 7 and tube formation assays of HUVECs after 6 h of Transwell cultivation. The qRT–PCR assay revealed that the mRNA expression of genes encoding angiopoietin 1 (ANGPT1), vascular endothelial growth factor (VEGF), and von Willebrand factor (vWF) was significantly upregulated in the BMP9 +HIF1α group compared with the other groups ($p < 0.05$). It is worth noting that the mRNA expression of ANGPT1, VEGF, and vWF was higher in the BMP9+Sim-Runx2 group than in the BMP9+ Sim-HIF1α group (Figure 2(a)).

The phenotypes of isolated HUVECs at the third passage were identified, and they highly expressed CD31, VEGF, EMCN, and vWF (Supplementary Figure 2). Tube formation assays showed that HIF1α significantly increased the relative tube area. Runx2 also increased the tube area, albeit to a lower degree than HIF1α, both independently and in combination with BMP9. Moreover, the relative tube area in the BMP9+Sim-HIF1α group was greatly decreased compared with that in the BMP9+ Sim-Runx2 group (Figures 2(b)–2(d)). Taken together, these data indicate that HIF1α and Runx2 are able to jointly regulate BMP9-induced angiogenic signaling and vascularization, and Runx2 may be an essential downstream target of HIF1α that participates in angiogenesis.

3.5. Effects of HIF1α and Runx2 on BMP9-Induced Vessel Invasion. To further investigate the effect of HIF1α and Runx2 on BMP9-induced angiogenesis *in vivo*, iMEFs were transfected with the appropriate adenovirus, seeded on PLGA scaffolds, and implanted in the dorsal subcutaneous tissue of male rats (Figure 5(a)). The cells adhered well to the PLGA scaffold after seeding for 72 h (Figure 5(b)). After gross observation of vascular invasion to the implants, PLGA scaffolds exhibited a vascularization effect, among which the vascularization ability in the BMP9 +HIF1α group was more apparent (Figure 5(c)). The implant histology demonstrated that PLGA scaffolds seeded with cells in the BMP9+HIF1α group showed greater levels of CD31 (Figure 5(d)). Remarkably, CD31 expression in the BMP9+Sim-Runx2 group was higher than that in the BMP9+ Sim-HIF1α group (Figure 5(e)). In summary, HIF1α significantly potentiated BMP9-induced angiogenesis *in vivo*, and silencing HIF1α inhibited the angiogenesis of iMEFs.

3.6. Runx2 Is Directly Upregulated by HIF1α in BMP9-Stimulated iMEFs. Our experiments confirmed that HIF1α and Runx2 are essential for osteoblastic differentiation of BMP9-stimulated iMEFs; therefore, we sought to determine whether HIF1α exerts any impact on BMP9-induced Runx2 expression. We used a ChIP assay to determine the relationship between HIF1α and Runx2 in BMP9 signaling. Gel electrophoresis was used to analyze the pulled down composite using an anti-HIF1α antibody, and the observed length was between 100 and 200 bp (Figure 6(a)). The location of promoter-specific primers for Runx2 yielded the expected products upon transfection with BMP9+HIF1α. We found pairs of primers targeting Runx2 that amplified the expected fragments in the group transfected with BMP9+HIF1α (Figure 6(b)). We further

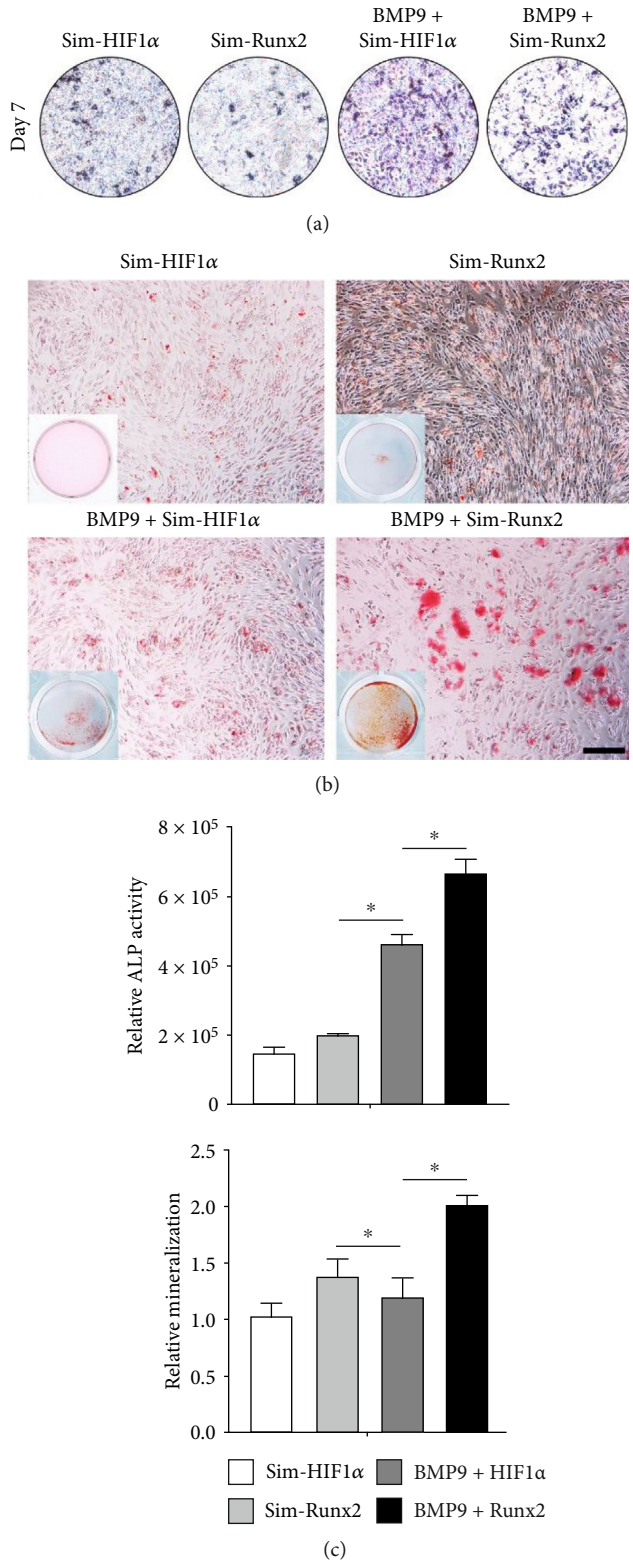

Figure 3: Silencing HIF1α and Runx2 effectively diminishes the BMP9-induced early osteogenic differentiation and late matrix mineralization of iMEFs. (a) Silencing HIF1α and Runx2 inhibited BMP9-induced ALP activity in iMEFs. (b) The matrix mineralization of iMEFs was evaluated by an Alizarin Red S staining assay. Representative gross images and microscopic images of cells subjected to the above treatments are shown after transfection. Alizarin Red S staining shows the effect of silencing HIF1α and Runx2 on BMP9-induced matrix mineralization in iMEFs (scale bar = 100 μm). (c) Quantification results showed that silencing HIF1α and Runx2 diminished BMP9-induced ALP activity and matrix mineralization, respectively ($^*p < 0.05$).

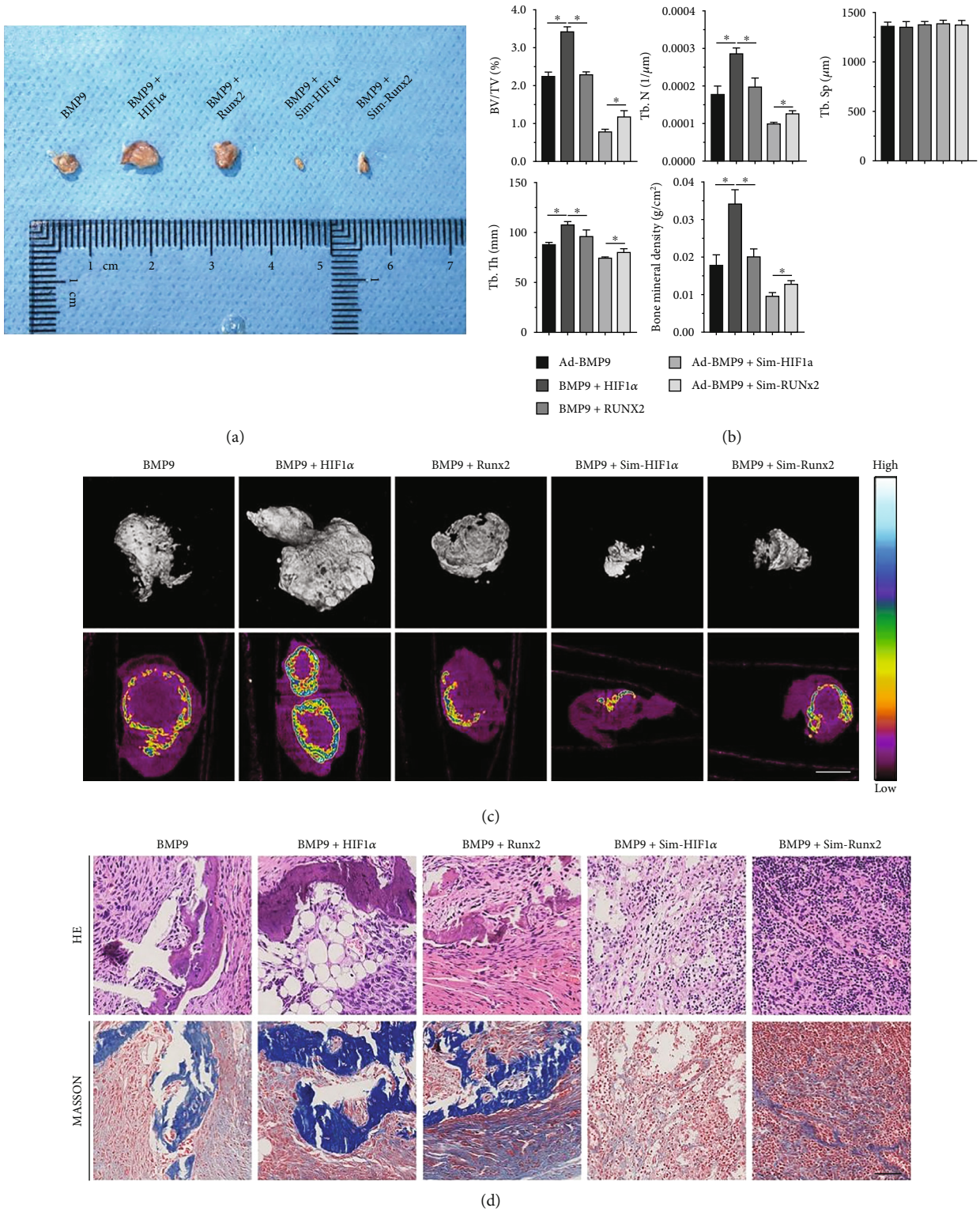

Figure 4: Effect of HIF1α and Runx2 on BMP9-induced ectopic osteogenesis after iMEF transplantation into nude mice. (a) BMP9-induced ectopic bone osteogenesis was enhanced by overexpression of HIF1α and Runx2 and inhibited by silencing HIF1α and Runx2. General observation of subcutaneous bone masses in nude mice. (b) Quantitative analysis of osteogenic masses and the relative values of BV/TV, Tb.N, Tb.Sp, Tb.Th, and bone mineral density (BMD) were analyzed ($^*p < 0.05$). (c) Subcutaneous osteogenic masses at 5 weeks were subjected to micro-CT analysis to investigate the 3D surface and generate a heatmap of average mineralization density. In the heatmap analysis, white represents the highest average mineral density, and black represents the lowest average mineral density (scale bar = 1 mm). (d) The retrieved samples were subjected to histologic staining, and the retrieved samples were fixed, decalcified, paraffin embedded, and subjected to H&E and Masson's trichrome staining (scale bar = 50 μm).

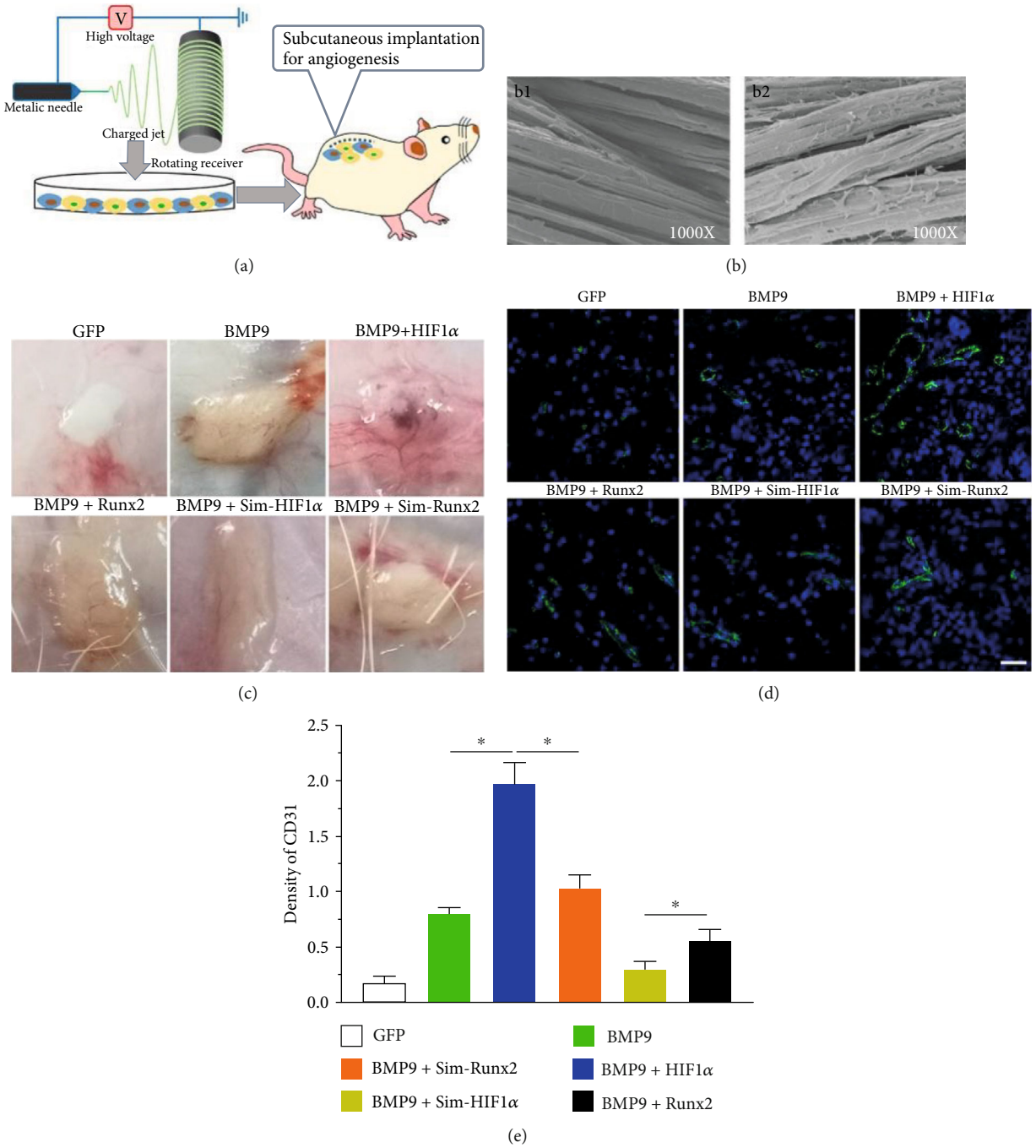

Figure 5: *In vivo* effects of the PLGA-transfected iMEF composite on vessel formation upon subcutaneous implantation into rats. (a) Schematic diagram showing the transfected iMEFs seeded on electrospun PLGA scaffolds implanted into the dorsal subcutaneous space of the mice. (b) Scanning electron microscopy image of the PLGA scaffold (b1) and seeded cells (b2) on the PLGA scaffold (magnification = 1000x). (c) General observation of harvested PLGA implants at 5 weeks. (d) Immunofluorescence staining for CD31 (vascular formation displays green fluorescence) and the average number of vascular structures in a high-power field for each implant (scale bar = 50 μm). (e) Quantification in each group is based on immunofluorescence staining.

determined the coupling effect between HIF1α and Runx2 at the transcription level by using a luciferase reporter assay. The results indicated that the transcriptional activity of the Runx2 luciferase reporter was significantly upregulated by HIF1α upon BMP9 stimulation for 48 hours (Figure 6(c)). However, the transcriptional activity of the HIF1α luciferase reporter gene was not obviously different upon Runx2 expression (Figure 6(d)). These data indicated that the transcription factor HIF1α can activate the promoter of Runx2 to regulate the initiation and activation of Runx2 at the gene transcription level, and the osteogenic differentiation induced by HIF1α and Runx2 may also be mediated by the activation of the BMP9-induced signaling pathway in iMEFs.

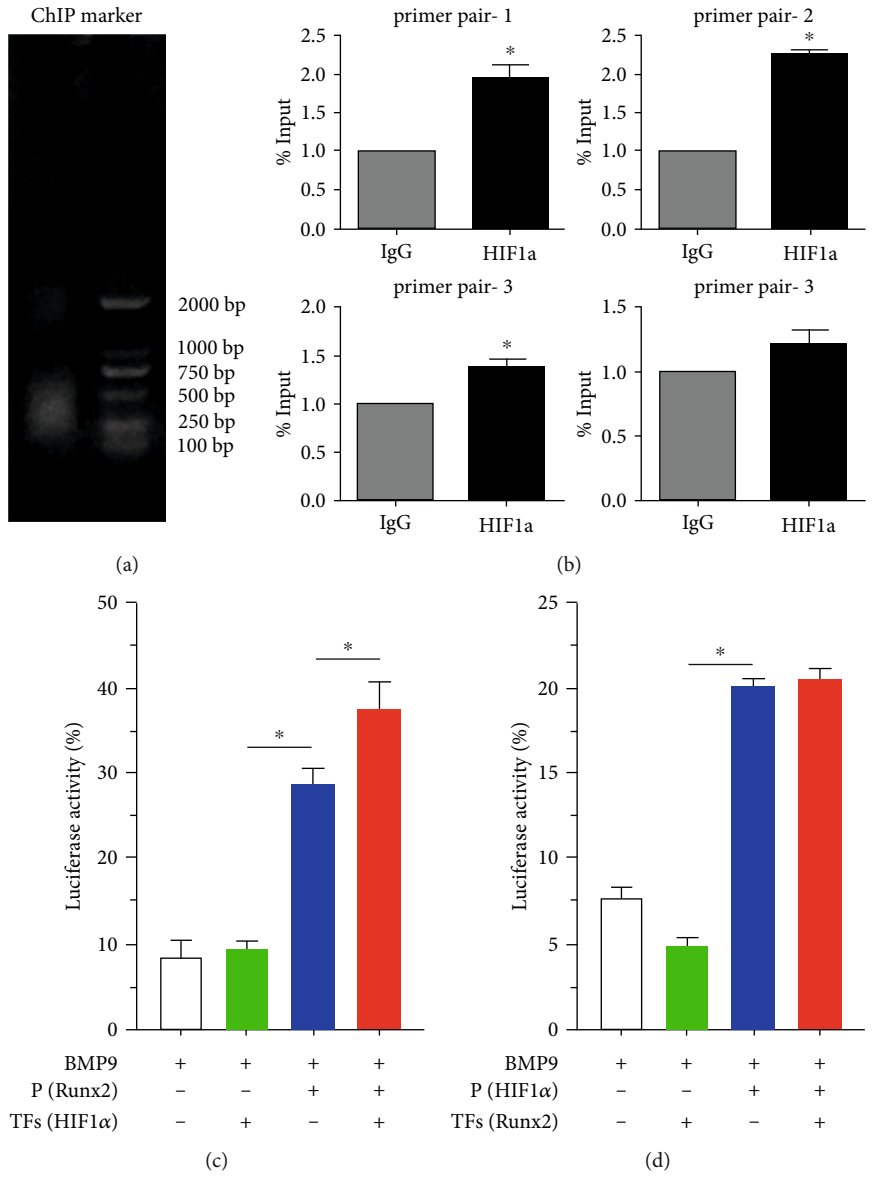

Figure 6: Identification and verification of Runx2 as an early downstream target of HIF1α enhanced by BMP9 in iMEFs. (a) ChIP analysis showed that Runx2 is a direct target of HIF1α signaling in iMEFs. iMEFs were transfected with Ad-BMP9 and Ad-HIF1α for 36 h, followed by formaldehyde crosslinking. The crosslinked cells were lysed and subjected to enzymolysis and immunoprecipitation with an anti-HIF1α or IgG antibody, the pulled down composite was subjected to gel electrophoresis and imaging, and primers for the Runx2 promoter region were used in the ChIP assay. (b) The recovered chromatin DNA fragments were used for qPCR amplification with 4 primers specific for the mouse Runx2 promoter. (c) Luciferase reporter assay results showed the effect of HIF1α and/or Runx2 on the transcriptional activities of the firefly/Renilla luminescence reporter. (d) The transcription factor Runx2 cannot activate the promoter of HIF1α. The transcription factor HIF1α can activate the promoter of Runx2 ($^*p < 0.05$).

4. Discussion

HIF1α is a well-established and vital regulator of angiogenesis, and it is necessary to elicit angiogenic signals to recruit new blood vessels and maintain many developmental processes, including skeletal development [26–28]. Runx2 is among the most vital transcription factors, is indispensable for osteogenic differentiation, and is responsible for the activation of osteogenesis marker genes [29, 30]. However, it remains unclear how HIF1α is coupled with Runx2 during the process of BMP9-induced osteogenic differentiation and bone formation. In this study, we explored whether HIF1α directly regulated Runx2 and whether HIF1α-mediated angiogenesis affected BMP9-stimulated osteogenic differentiation of MPCs. We detected the effect of HIF1α and Runx2 on ALP activity as an early osteogenic factor, bone mineralization as a late osteogenic indicator, the expression of osteogenesis- and angiogenesis-related factors and consolidated subcutaneous ectopic bone formation of iMEFs in athymic nude mice, increased osteogenic volume, and the values of BV/TV, Tb.Th, Tb.N, and BMD; we also investigated HUVEC tube formation in prevascular-like structures

after *in vitro* and *in vivo* PLGA subcutaneous implantation for angiopoiesis. Overall, the results demonstrated that the exogenous expression of HIF1α and Runx2 enhances BMP9-stimulated osteogenic differentiation, including ALP activity, calcium deposition, and the expression of osteogenesis-related factors such as BSP, COL-A1, OPN, and ectopic subcutaneous bone formation, yet silencing HIF1α and/or Runx2 strongly blocked BMP9-induced osteogenic signaling in iMEFs. Furthermore, while stable overexpression of HIF1α and Runx2 can potentiate the angiogenesis-related factors ANGPT1, VEGF, and vWF and support HUVEC orientation into prevascular-like structures *in vitro* and intensify robust vascularization in ectopic subcutaneous implantation of PLGA-transfected iMEFs, silencing HIF1α and Runx2 can profoundly inhibit these effects *in vitro* and *in vivo*. Mechanistically, HIF1α can directly regulate the activation of Runx2 at the transcriptional level, and HIF1α also exerts a synergistic effect by promoting angiogenic and osteogenic signaling pathways upon BMP9 induction in iMEFs. Therefore, our results strongly demonstrate that the coupling between HIF1α and Runx2 plays an essential role in BMP9-induced osteogenic and angiogenic differentiation.

HIF1α is a well-established factor that regulates adaptive responses, including capillary ingrowth and angiogenesis, to reduce oxygen utilization, both spatially and temporally. It was previously reported that oxygen-sensitive HIFα subunits are found in mammals: HIF1α, HIF2α, and HIF3α. HIF1α and HIF2α have been widely studied and are the most common [31]. There are two regulatory models of HIF1α. Under normoxia, HIF1α is rapidly hydroxylated and ubiquitinated by the E3 ubiquitin ligase complex, which contains the von Hippel-Lindau disease tumor suppressor (VHL) protein and undergoes rapid degradation. Another regulatory model of HIF1α is that HIF1α is hydroxylated at asparagine residues by inhibiting the HIF1 factor to prevent the transcriptional activity of HIF1α, which is accomplished by blocking the interaction of the transcriptional coactivator cAMP response element binding protein (CBP) and histone acetyltransferase p 300 (P 300 HAT) with HIF1α [32, 33]. In contrast, under hypoxic conditions, HIF1α is stabilized by limited oxygen as a helper substrate for prolyl hydroxylase domain enzymes (PHDs), and the HIF1α protein hydroxylation rate is reduced by enhancing the transcriptional activation of PHD, HIF1, and CBP-p 300 coactivated complexes. Then, HIFα levels increase, and HIF1α target genes are expressed [34, 35]. Recent studies have shown that stimulating angiogenesis plays a key role in the process of increased bone mass while the HIF1α-VEGF pathway is activated [33]. Some research found that VEGF enhances BMP-mediated stimulation of anabolic bone formation by affecting angiogenesis [36–38]. The possible nonautonomous mechanisms underlying the overexpression of HIF1α in mature mouse osteoblasts include the possibility that blocking the VHL protein significantly enhances angiogenesis and osteogenesis, including the activation of VEGF in vascular endothelial cells. Hence, in mice lacking HIF-1α, the trabecular bone volume and bone formation rate were significantly reduced, the cortical bone structure was changed, and vascular development in the long bones was decreased [39]. Our study

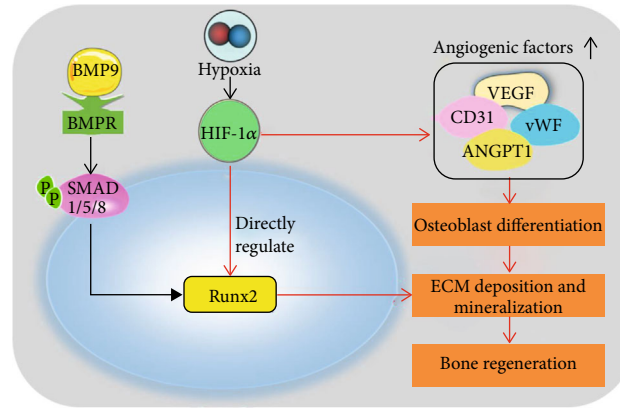

Figure 7: Proposed regulatory loop involving BMP9, HIF1α, and Runx2 in iMEFs. Runx2 and osteogenic marker factors are upregulated by BMP9 through BMP/Smad1/5/8 signaling to promote osteogenesis. A hypoxic environment leads to elevated HIF1α levels, which directly regulate the transcriptional function of Runx2 in the nucleus. Runx2 is an important target of HIF1α in iMEFs that regulates osteogenic differentiation *in vitro* and *in vivo*. Another possible important branch of the regulatory loop between HIF1α and osteogenesis is that HIF1α is a vital factor that plays a positive role in vascularization by regulating the expression of vasoformation-related regulators, including VEGF, CD31, vWF, and ANGPT1. Our initial results support the notion that the transcript activity of Runx2 is regulated by and coupled to HIF1α, which is enhanced by BMP9. This loop not only strengthens the osteogenic differentiation of iMEFs and angiogenesis mediated by HIF1α but also enhances extracellular matrix deposition and mineralization, which boosts efficient bone regeneration.

showed that overexpression of exogenous HIF1α intensified BMP9-induced osteogenic differentiation and osteogenesis. Angiogenesis-related factors (e.g., VEGF, ANGPT1, CD31, and vWF) were upregulated, and the activity of prevascular structures and subcutaneous vasoformation were higher in the HIF1α-expressing group.

In contrast, silencing HIF1α impaired the osteoblast and angiogenic differentiation ability, as observed in the cells treated with Sim-HIF1α. Therefore, HIF1α signaling in anabolic bone formation may increase osteogenesis via a cell-nonautonomous effect to integrate spatiotemporal expansion and revascularization and establishment of the blood supply in bone, although it does not preclude the existence of additional effectors. Moreover, we believe that HIF1α signaling is a critical accommodator of new vessels for bone regeneration.

Runx2 belongs to the small transcription factor family, and members of the Runx family contain the runt domain [40]. Runx2 is a vital regulator in bone development and is essential for osteoblast differentiation. Mutation of Runx2 is related to skeletal malformation syndromes, including cleidocranial dysplasia (CCD) [41, 42]. Runx2 knockout mice lose all intramembranous and endochondral osteogenesis and die after birth due to lack of mineralization in the chest region, which results in breathing difficulties, even in the presence of BMP [43]. The DNA sequence 5′-PuACCPuCA-3′ and its complementary sequence 5′-TGPyGGTPy-3′ are recognized

by Runx2, which is capable of binding to the promoters of genes encoding type I collagen, osteopontin, osteocalcin, BSP, collagenase-3, VEGF, type X collagen, and others to enhance the expression of these proteins and boost the osteoblastic differentiation [44–47]. These results may indicate that Runx2 is important for regulating osteogenesis, chondrocyte hypertrophy, and vascular invasion of the developing skeleton [15, 48]. Our results revealed that Runx2 overexpression is capable of promoting BMP9-induced early and late osteogenesis and ectopic subcutaneous bone formation and upregulating the expression of osteogenesis- and angiogenesis-related genes. In addition, Runx2 organizes HUVECs into prevascular-like structures *in vitro* and promotes vascularization *in vivo* after PLGA implantation, even though Runx2-mediated osteogenesis and angiogenesis were less robust than those induced by HIF1α. Conversely, silencing Runx2 attenuated the effects of BMP9-stimulated osteogenesis and angiogenesis, further confirming that Runx2 is a key regulator of osteoblastic and angiopoietic differentiation and a molecular transducer in osteogenic biology.

Even though bone formation is primarily mediated by osteoblasts, many other tissues in bone consist of vascular endothelium and/or sensory and motor nerves that help establish a conducive milieu for bone formation [49–54]. Our *in vitro* HUVEC tube formation assays and *in vivo* analysis of angiogenesis after PLGA implantation showed that the level of CD31 was increased by overexpression of HIF1α and Runx2. Furthermore, the expression of angiogenic-related factors was higher after overexpressing HIF1α than that elicited by Runx2, and silencing HIF1α decreased the expression of these factors to a greater degree than did inhibiting Runx2.

We further evaluated the relationship between HIF1α and Runx2 at the gene level. Luciferase reporter assays showed that the transcription factor HIF1α was able to enhance luciferase expression downstream of the Runx2 promoter. The mRNA of Runx2 was shown to be pulled down with an anti-HIF1α antibody. Mechanistically, these data demonstrated that Runx2 is a downstream target of HIF1α and that HIF1α can directly regulate Runx2 (Figure 7).

5. Conclusion

In summary, this study recognized the ability of HIF1α and Runx2 to stimulate osteogenic and angiogenic differentiation of iMEFs and showed that silencing HIF1α and Runx2 inhibited BMP signaling. The coupling effect of HIF1α and Runx2 may play an essential role in osteogenic and angiogenic pathways during the process of bone formation in BMP9-induced iMEFs. In our study, only adenoviruses were used to upregulate and downregulate exogenous expression of HIF1α and Runx2, but in clinical applications, adenoviruses must meet a higher standard. It is possible to use adenoviruses in animal models, but they have not yet been used in clinical applications. Additionally, the exact mechanism by which HIF1α and Runx2 regulate BMP9-induced effects in iMEFs and vascular endothelial cells remains unclear and needs further study.

Abbreviations

AHR: Aryl-hydrocarbon receptor
ANGPT1: Angiopoietin 1
BMD: Bone mineral density
BMP9: Bone morphogenetic protein 9
BMPs: Bone morphogenetic proteins
BMSCs: Bone marrow stromal cells
BSP: Bone sialoprotein
CBP: cAMP response element-binding protein
CCD: Cleidocranial dysplasia
ChIP: Chromatin immunoprecipitation assays
COL-A1: Collagen type I
COX-2: Cytochrome c oxidase subunit II
ECM: Endothelial conditioned medium
EMCN: Endomucin
FBS: Fetal bovine serum
GFP: Green fluorescent protein
H&E: Hematoxylin and eosin
Hey1: Hes-related family bHLH transcription factor with YRPW motif 1
HIF1α: Hypoxia-inducible factor 1α
HUVECs: Human umbilical vein endothelial cells
iMEF: Immortalized mouse embryonic fibroblast
MPCs: Mesenchymal progenitor cells
OPN: Osteopontin
PHD: Prolyl hydroxylase domain enzymes
PLGA: Poly(lactic-co-glycolic acid
qRT-PCR: Quantitative reverse transcription polymerase chain reaction
RFP: Red fluorescent protein
Runx2: Runt-related transcription factor 2
TGF-β: Transforming growth factor beta
VEGF: Vascular endothelial growth factor
VHL: von Hippel-Lindau disease tumor suppressor
vWF: von Willebrand factor.

Data Availability

All data generated or analyzed during this study are included in this published article (and its supplementary information files).

Ethical Approval

This study was approved by the Research Ethics Committee of the First Affiliated Hospital of Chongqing Medical University (No. 160301).

Conflicts of Interest

The authors declare that they have no conflicts of interest.

Authors' Contributions

Y.L. and Z.L. designed the experiments. Y.L., Z.L., H.W., J.Z., M.L., Y.W., and Y.J. performed the experiments. Y.L. and J.H. performed the statistical analysis. Y.L. and Z.L. wrote the manuscript. Y.A. conceived of the study and participated in its design and coordination. All

authors read and approved the final manuscript. Yuwan Li and Ziming Liu contributed equally to this work.

Acknowledgments

This work was supported by the China Postdoctoral Science Foundation (No. 2020M680258).

Supplementary Materials

Supplementary Figure 1 The recombinant adenovirus Ad-GFP (green), Ad-BMP9 (green), Ad-HIF1α (red), Ad-Sim-HIF1α (red), Ad-Runx2 (red), and Ad-Sim-Runx2 (red) were effectively transfected into iMEFs as observed by fluorescence microscopy (scale bar = 100 μm). Supplementary Figure 2: phenotype and identification of HUVECs. Immunofluorescence staining assay of the typical biomarkers of CD31, VEGF, EMCN, and vWF of HUVECs (scale bar = 100 μm). Supplementary Table 1: oligonucleotides used for ChIP amplicon. Supplementary Table 2: the promoter sequence of Runx2. *(Supplementary Materials)*

References

[1] D. J. Prockop, "Marrow stromal cells as stem cells for nonhematopoietic tissues," *Science*, vol. 276, no. 5309, pp. 71–74, 1997.

[2] M. F. Pittenger, A. M. Mackay, S. C. Beck et al., "Multilineage potential of adult human mesenchymal stem cells," *Science*, vol. 284, no. 5411, pp. 143–147, 1999.

[3] E. Ubil, J. Duan, I. C. Pillai et al., "Mesenchymal-endothelial transition contributes to cardiac neovascularization," *Nature*, vol. 514, no. 7524, pp. 585–590, 2014.

[4] M. Kassem and P. Bianco, "Skeletal stem cells in space and time," *Cell*, vol. 160, no. 1-2, pp. 17–19, 2015.

[5] I. Prieto, A. Zambrano, J. Laso, A. Aranda, E. Samper, and M. Monsalve, "Early induction of senescence and immortalization in PGC-1α-deficient mouse embryonic fibroblasts," *Free Radical Biology & Medicine*, vol. 138, pp. 23–32, 2019.

[6] E. Huang, Y. Bi, W. Jiang et al., "Conditionally immortalized mouse embryonic fibroblasts retain proliferative activity without compromising multipotent differentiation potential," *PLoS One*, vol. 7, no. 2, article e32428, 2012.

[7] I. Prieto, C. R. Alarcon, R. Garcia-Gomez et al., "Metabolic adaptations in spontaneously immortalized PGC-1α knockout mouse embryonic fibroblasts increase their oncogenic potential," *Redox Biology*, vol. 29, article 101396, 2020.

[8] S. S. Lange, J. Tomida, K. S. Boulware, S. Bhetawal, and R. D. Wood, "The polymerase activity of mammalian DNA pol ζ is specifically required for cell and embryonic viability," *PLoS Genetics*, vol. 12, no. 1, article e1005759, 2016.

[9] S. Ceccariglia, A. Cargnoni, A. R. Silini, and O. Parolini, "Autophagy: a potential key contributor to the therapeutic action of mesenchymal stem cells," *Autophagy*, vol. 16, no. 1, pp. 28–37, 2020.

[10] A. Brauer, T. Pohlemann, and W. Metzger, "Osteogenic differentiation of immature osteoblasts: interplay of cell culture media and supplements," *Biotechnic & Histochemistry*, vol. 91, no. 3, pp. 161–169, 2016.

[11] T. Katagiri, S. Tsukamoto, Y. Nakachi, and M. Kuratani, "Discovery of heterotopic bone-inducing activity in hard tissues and the TGF-β superfamily," *International Journal of Molecular Sciences*, vol. 19, no. 11, p. 3586, 2018.

[12] N. Duval, C. Vaslin, T. Barata et al., "BMP4 patterns Smad activity and generates stereotyped cell fate organisation in spinal organoids," *Development*, vol. 146, no. 14, article dev175430, 2019.

[13] J. D. Lamplot, J. Qin, G. Nan et al., "BMP9 signaling in stem cell differentiation and osteogenesis," *American Journal of Stem Cells*, vol. 2, no. 1, pp. 1–21, 2013.

[14] N. Hu, D. Jiang, E. Huang et al., "BMP9-regulated angiogenic signaling plays an important role in the osteogenic differentiation of mesenchymal progenitor cells," *Journal of Cell Science*, vol. 126, no. 2, pp. 532–541, 2013.

[15] M. Z. Liu, D. C. Zhou, Q. Liu et al., "Osteogenesis activity of isocoumarin a through the activation of the PI3K-Akt/Erk cascade-activated BMP/RUNX2 signaling pathway," *European Journal of Pharmacology*, vol. 858, article 172480, 2019.

[16] K. A. Sharff, W. X. Song, X. Luo et al., "Hey1 basic helix-loop-helix protein plays an important role in mediating BMP9-induced osteogenic differentiation of mesenchymal progenitor cells∗," *The Journal of Biological Chemistry*, vol. 284, no. 1, pp. 649–659, 2009.

[17] R. Ren, P. C. Charles, C. Zhang, Y. Wu, H. Wang, and C. Patterson, "Gene expression profiles identify a role for cyclooxygenase 2-dependent prostanoid generation in BMP6-induced angiogenic responses," *Blood*, vol. 109, no. 7, pp. 2847–2853, 2007.

[18] T. C. He, S. Zhou, L. T. da Costa, J. Yu, K. W. Kinzler, and B. Vogelstein, "A simplified system for generating recombinant adenoviruses," *Proceedings of the National Academy of Sciences of the United States of America*, vol. 95, no. 5, pp. 2509–2514, 1998.

[19] J. Luo, Z. L. Deng, X. Luo et al., "A protocol for rapid generation of recombinant adenoviruses using the AdEasy system," *Nature Protocols*, vol. 2, no. 5, pp. 1236–1247, 2007.

[20] J. Cui, W. Zhang, E. Huang et al., "BMP9-induced osteoblastic differentiation requires functional notch signaling in mesenchymal stem cells," *Laboratory Investigation*, vol. 99, no. 1, pp. 58–71, 2019.

[21] S. Lu, J. Wang, J. Ye et al., "Bone morphogenetic protein 9 (BMP9) induces effective bone formation from reversibly immortalized multipotent adipose-derived (iMAD) mesenchymal stem cells," *American Journal of Translational Research*, vol. 8, no. 9, pp. 3710–3730, 2016.

[22] M. Yang, Z. Liang, M. Yang et al., "Role of bone morphogenetic protein-9 in the regulation of glucose and lipid metabolism," *The FASEB Journal*, vol. 33, no. 9, pp. 10077–10088, 2019.

[23] Y. Shao, Q. Z. Chen, Y. H. Zeng et al., "All-trans retinoic acid shifts rosiglitazone-induced adipogenic differentiation to osteogenic differentiation in mouse embryonic fibroblasts," *International Journal of Molecular Medicine*, vol. 38, no. 6, pp. 1693–1702, 2016.

[24] N. Tang, W. X. Song, J. Luo et al., "BMP-9-induced osteogenic differentiation of mesenchymal progenitors requires functional canonical Wnt/β-catenin signalling," *Journal of Cellular and Molecular Medicine*, vol. 13, no. 8B, pp. 2448–2464, 2009.

[25] L. Chen, W. Jiang, J. Huang et al., "Insulin-like growth factor 2 (IGF-2) potentiates BMP-9-induced osteogenic differentiation and bone formation," *Journal of Bone and Mineral Research*, vol. 25, no. 11, pp. 2447–2459, 2010.

[26] T. Tando, Y. Sato, K. Miyamoto et al., "Hif1α is required for osteoclast activation and bone loss in male osteoporosis," *Biochemical and Biophysical Research Communications*, vol. 470, no. 2, pp. 391–396, 2016.

[27] K. Wang, L. Le, B. M. Chun et al., "A novel osteogenic cell line that differentiates into GFP-tagged osteocytes and forms mineral with a bone-like lacunocanalicular structure," *Journal of Bone and Mineral Research*, vol. 34, no. 6, pp. 979–995, 2019.

[28] X. Chen, S. Gu, B. F. Chen et al., "Nanoparticle delivery of stable miR-199a-5p agomir improves the osteogenesis of human mesenchymal stem cells via the HIF1a pathway," *Biomaterials*, vol. 53, pp. 239–250, 2015.

[29] S. Vimalraj, B. Arumugam, P. J. Miranda, and N. Selvamurugan, "Runx2: structure, function, and phosphorylation in osteoblast differentiation," *International Journal of Biological Macromolecules*, vol. 78, pp. 202–208, 2015.

[30] Y. Ikebuchi, S. Aoki, M. Honma et al., "Coupling of bone resorption and formation by RANKL reverse signalling," *Nature*, vol. 561, no. 7722, pp. 195–200, 2018.

[31] L. Ravenna, L. Salvatori, and M. A. Russo, "HIF3α: the little we know," *The FEBS Journal*, vol. 283, no. 6, pp. 993–1003, 2016.

[32] K. Lisy and D. J. Peet, "Turn me on: regulating HIF transcriptional activity," *Cell Death and Differentiation*, vol. 15, no. 4, pp. 642–649, 2008.

[33] C. Wan, J. Shao, S. R. Gilbert et al., "Role of HIF-1α in skeletal development," *Annals of the New York Academy of Sciences*, vol. 1192, no. 1, pp. 322–326, 2010.

[34] P. H. Maxwell, M. S. Wiesener, G. W. Chang et al., "The tumour suppressor protein VHL targets hypoxia-inducible factors for oxygen-dependent proteolysis," *Nature*, vol. 399, no. 6733, pp. 271–275, 1999.

[35] P. Jaakkola, D. R. Mole, Y. M. Tian et al., "Targeting of HIF-α to the von Hippel-Lindau ubiquitylation complex by O2-regulated prolyl hydroxylation," *Science*, vol. 292, no. 5516, pp. 468–472, 2001.

[36] H. Aksel, S. Ozturk, A. Serper, and K. Ulubayram, "VEGF/BMP-2 loaded three-dimensional model for enhanced angiogenic and odontogenic potential of dental pulp stem cells," *International Endodontic Journal*, vol. 51, no. 4, pp. 420–430, 2018.

[37] W. Zhang, C. Zhu, Y. Wu et al., "VEGF and BMP-2 promote bone regeneration by facilitating bone marrow stem cell homing and differentiation," *European Cells & Materials*, vol. 27, p. 1, 2014.

[38] G. An, W. B. Zhang, D. K. Ma et al., "Influence of VEGF/BMP-2 on the proliferation and osteogenetic differentiation of rat bone mesenchymal stem cells on PLGA/gelatin composite scaffold," *European Review for Medical and Pharmacological Sciences*, vol. 21, no. 10, pp. 2316–2328, 2017.

[39] S. H. Shomento, C. Wan, X. Cao et al., "Hypoxia-inducible factors 1α and 2α exert both distinct and overlapping functions in long bone development," *Journal of Cellular Biochemistry*, vol. 109, no. 1, pp. 196–204, 2010.

[40] J. Rennert, J. A. Coffman, A. R. Mushegian, and A. J. Robertson, "The evolution of Runx genes I. a comparative study of sequences from phylogenetically diverse model organisms," *BMC Evolutionary Biology*, vol. 3, no. 1, p. 4, 2003.

[41] E. Hordyjewska-Kowalczyk, A. Sowinska-Seidler, E. M. Olech et al., "Functional analysis of novel RUNX2 mutations identified in patients with cleidocranial dysplasia," *Clinical Genetics*, vol. 96, no. 5, pp. 429–438, 2019.

[42] A. Jaruga, E. Hordyjewska, G. Kandzierski, and P. Tylzanowski, "Cleidocranial dysplasia and RUNX2-clinical phenotype–genotype correlation," *Clinical Genetics*, vol. 90, no. 5, pp. 393–402, 2016.

[43] H. Kobayashi, Y. Gao, C. Ueta, A. Yamaguchi, and T. Komori, "Multilineage differentiation of _Cbfa1_ -deficient calvarial cells _in vitro_," *Biochemical and Biophysical Research Communications*, vol. 273, no. 2, pp. 630–636, 2000.

[44] T. Komori, "Roles of Runx2 in skeletal development," *Advances in Experimental Medicine and Biology*, vol. 962, pp. 83–93, 2017.

[45] A. M. Buo, R. E. Tomlinson, E. R. Eidelman, M. Chason, and J. P. Stains, "Connexin43 and Runx2 interact to affect cortical bone geometry, skeletal development, and osteoblast and osteoclast function," *Journal of Bone and Mineral Research*, vol. 32, no. 8, pp. 1727–1738, 2017.

[46] K. Nakashima, X. Zhou, G. Kunkel et al., "The novel zinc finger-containing transcription factor osterix is required for osteoblast differentiation and bone formation," *Cell*, vol. 108, no. 1, pp. 17–29, 2002.

[47] C. M. Martins, I. O. de Azevedo Queiroz, E. Ervolino, L. T. A. Cintra, and J. E. Gomes-Filho, "RUNX-2, OPN and OCN expression induced by grey and white mineral trioxide aggregate in normal and hypertensive rats," *International Endodontic Journal*, vol. 51, no. 6, pp. 641–648, 2018.

[48] A. Narayanan, N. Srinaath, M. Rohini, and N. Selvamurugan, "Regulation of Runx2 by microRNAs in osteoblast differentiation," *Life Sciences*, vol. 232, article 116676, 2019.

[49] T. Fukuda, S. Takeda, R. Xu et al., "Sema3A regulates bone-mass accrual through sensory innervations," *Nature*, vol. 497, no. 7450, pp. 490–493, 2013.

[50] Y. Zhang, J. Xu, Y. C. Ruan et al., "Implant-derived magnesium induces local neuronal production of CGRP to improve bone-fracture healing in rats," *Nature Medicine*, vol. 22, no. 10, pp. 1160–1169, 2016.

[51] B. F. Boyce, "Sphingosine-1 phosphate: a new player in osteoimmunology," *Developmental Cell*, vol. 16, no. 3, pp. 323-324, 2009.

[52] P. Dimitri and C. Rosen, "The central nervous system and bone metabolism: an evolving story," *Calcified Tissue International*, vol. 100, no. 5, pp. 476–485, 2017.

[53] S. Nencini, M. Ringuet, D. H. Kim, Y. J. Chen, C. Greenhill, and J. J. Ivanusic, "Mechanisms of nerve growth factor signaling in bone nociceptors and in an animal model of inflammatory bone pain," *Molecular Pain*, vol. 13, p. 174480691769701, 2017.

[54] C. O. Frost, R. R. Hansen, and A. M. Heegaard, "Bone pain: current and future treatments," *Current Opinion in Pharmacology*, vol. 28, pp. 31–37, 2016.

Hindawi
BioMed Research International
Volume 2023, Article ID 9765196, 1 page
https://doi.org/10.1155/2023/9765196

Retraction

Retracted: Gastrocnemius Muscle Injury Is the Condition to Induce Cartilage Degeneration of the Rabbit Tibiofemoral Joint: A New Perspective

BioMed Research International

Received 26 September 2023; Accepted 26 September 2023; Published 27 September 2023

This article has been retracted by Hindawi following an investigation undertaken by the publisher [1]. This investigation has uncovered evidence of one or more of the following indicators of systematic manipulation of the publication process:

(1) Discrepancies in scope

(2) Discrepancies in the description of the research reported

(3) Discrepancies between the availability of data and the research described

(4) Inappropriate citations

(5) Incoherent, meaningless and/or irrelevant content included in the article

(6) Peer-review manipulation

The presence of these indicators undermines our confidence in the integrity of the article's content and we cannot, therefore, vouch for its reliability. Please note that this notice is intended solely to alert readers that the content of this article is unreliable. We have not investigated whether authors were aware of or involved in the systematic manipulation of the publication process.

In addition, our investigation has also shown that one or more of the following human-subject reporting requirements has not been met in this article: ethical approval by an Institutional Review Board (IRB) committee or equivalent, patient/participant consent to participate, and/or agreement to publish patient/participant details (where relevant).

Wiley and Hindawi regrets that the usual quality checks did not identify these issues before publication and have since put additional measures in place to safeguard research integrity.

We wish to credit our own Research Integrity and Research Publishing teams and anonymous and named external researchers and research integrity experts for contributing to this investigation.

The corresponding author, as the representative of all authors, has been given the opportunity to register their agreement or disagreement to this retraction. We have kept a record of any response received.

References

[1] Y. Li, J. Sun, Y. Hou et al., "Gastrocnemius Muscle Injury Is the Condition to Induce Cartilage Degeneration of the Rabbit Tibiofemoral Joint: A New Perspective," *BioMed Research International*, vol. 2022, Article ID 7532434, 12 pages, 2022.

Hindawi
BioMed Research International
Volume 2022, Article ID 7532434, 12 pages
https://doi.org/10.1155/2022/7532434

Research Article

Gastrocnemius Muscle Injury Is the Condition to Induce Cartilage Degeneration of the Rabbit Tibiofemoral Joint: A New Perspective

Yuanyuan Li, Jiwei Sun, Yimin Hou, Jiabi Wei, Yuzhuo Chai, Xiangyu Zhu, and Rongguo Wang

School of Acupuncture-Moxibustion and Tuina, Beijing University of Chinese Medicine, Fangshan District, Beijing, China

Correspondence should be addressed to Rongguo Wang; wgls2001@163.com

Received 28 July 2022; Accepted 20 August 2022; Published 2 September 2022

Academic Editor: Alok Raghav

The knee osteoarthritis is a common joint disease that causes pain and inconvenience. Clinically, patients with knee osteoarthritis often have response points on the gastrocnemius. Gastrocnemius plays an essential role in stabilizing joints and changing gait and pace, which also has a close relationship with the knee joint. The objective of this study is to determine changes in the tibiofemoral joint after medial and lateral gastrocnemius injury. Rabbits were divided into a medial gastrocnemius injury group, a lateral gastrocnemius injury group, and a control group with two intervals: 6 and 8 weeks after modeling of the semisevered gastrocnemius. The gastrocnemius was weighed and sectioned for histology. The joint space and subchondral bone were observed using X-ray and microcomputed tomography. The cartilage was observed histologically using Safranin O fast green and Masson and immunohistochemically using antibodies to collagen type II, matrix metalloproteinase 13, and integrin beta1. Results showed muscle fiber atrophy, and fibrotic changes occurred after gastrocnemius semidissociation. After gastrocnemius injury, the femoral condyle of the tibiofemoral joint produced abnormal sclerosis and bone degeneration. The pathological changes of cartilage included disordered or reduced cell alignment, cartilage matrix loss, and collagen loss due to decreased collagen type II and increased matrix metalloproteinase 13 activity. The increase of integrin beta1 in the injured group may be related to mechanical conduction process. The results suggest that gastrocnemius injury is an essential factor in tibiofemoral arthritis.

1. Introduction

Osteoarthritis is a common disabling total joint disease characterized by pain and personal and socioeconomic burdens. The knee joint is the most common site [1]. Knee osteoarthritis (KOA) results from the interaction of multifactorial, complex structural, and mechanical factors; the preferred treatment is nonsurgical, with ameliorable risk factors as the target [2]. Strengthening the muscles around the knee joint is highly recommended for prevention and early treatment; however, the specific exercise methods vary [3]. This is because biomechanical factors, including muscle tension in the thighs and alignment imbalance in the lower limbs, play essential roles in the initiation of KOA [4]. Studies showed that KOA might lead to atrophy of the quadriceps femoris muscle [5], and the increase in quadriceps strength is beneficial for functional activities and alleviating the pain associated with KOA [6]. Hamstring coactivation may attenuate measures of quadriceps strength in a gender-dependent manner [7]. Nevertheless, little attention has been paid to the associations between calf muscles and KOA.

The diagnosis and treatment of KOA begin with identifying gastrocnemius tenderness, and palpable cords are often present on palpation of the calf. The gastrocnemius spans the knee, ankle, and subtalus joints. It plays an essential role in maintaining gait balance in the lower limbs, stabilizing joints, and changing gait and pace [8]. The gastrocnemius is divided into medial and lateral heads that differ in morphology and function [9, 10]. Excessive activation of the medial and lateral gastrocnemius leads to limited dorsiflexion of the

ankle joint, and this may be one of the essential mechanisms leading to medial knee displacement [11, 12]. The posterior side of the knee joint is the most frequently loaded and tensioned part of the knee joint; a study showed that during the gait cycle, when the foot follows the ground to the toe off the ground, the knee joint reaction force is the largest, the gastrocnemius force reaches a peak, and the period of gastrocnemius contraction is relatively large [13]. The gastrocnemius and hamstring muscles are essential flexors in the posterior part of the knee joint, and their activation is correlated with the improvement of gait in patients with KOA [14]. Gastrocnemius muscle injury is common and is often related to the crossing of two joints [15].

Articular cartilage is the first layer of structure to experience joint stress, and collagen type II (Col-II) is the largest fraction of the solid matrix remaining in the extracellular matrix of the cartilage other than water [16, 17]. The essential change after cartilage injury is the reduction of type II collagen by enzymatic hydrolysis. Matrix metalloproteinase 13 (MMP13) has higher activity against COL-II than other collagens and is the central node of the cartilage degradation pathway [18]. The occurrence of knee osteoarthritis is verified by observing whether the femoral condyle tissue shows a decreased expression of Col-II and the presence of MMP13 activity. Integrin is a mechanical sensitive factor, among which beta1 subtype plays an important role in cartilage mechanical conduction [19]. The content of integrin beta1 (ITG-β1) was measured to observe whether the mechanical changes of cartilage were caused by gastrocnemius injury and the level of mechanical factors was changed. Furthermore, the gastrocnemius injury varies because of differences in the function of the medial gastrocnemius (MG) and lateral gastrocnemius (LG), commonly leading to arthritis. Nevertheless, there has been no discussion concerning the relationship of gastrocnemius injury to knee joint degeneration.

Therefore, we hypothesized that gastrocnemius injury would cause pathological changes in cartilage and subchondral bone of the tibiofemoral joint that may progress to KOA. The objective was to provide evidence that gastrocnemius injury causes KOA and provide a conceptual basis for the prevention and treatment of KOA.

2. Materials and Methods

2.1. Animal Model. The Animal Ethics Committee at Beijing University of Chinese Medicine approved the animal experiments (Ethics Reference No. BUCM–4–2020112003-4070). We used 36 male New Zealand white rabbits (weight 2.19 ± 0.13 kg) provided by Fulong Tengfei Experimental Animal Co., Ltd. All rabbits drank distilled water freely, were fed at regular intervals, and were maintained in a suitable environment (20–25°C, 50%–70% relative humidity; clean and quiet). The rabbits were adapted to the experimental feeding environment for 1 week and then randomly divided into the control (CON) group ($n = 6$), medial gastrocnemius injury (MGI) group ($n = 6$), and lateral gastrocnemius injury (LGI) groups ($n = 6$). In the control group, the right legs were not treated. In the MGI group, part of the muscle of MG of the right leg was incised with a special scalpel, and the LG muscle was cut in the LGI group. No animals underwent procedures on the left leg. All were fed normally after the procedure and were driven to run for 2 hours a day. The animals were sacrificed by administering overdoses of Zoletil®50 (3 ml/kg) in the auricular vein at 6 and 8 weeks after surgery. Specimens of gastrocnemius and knee femoral condyle were collected.

2.2. Surgical Technique. The surgical tool was a custom-made tungsten steel scalpel (AN6418-01, Beijing Zhongyan Taihe Medical Instrument, China) (Figure 1). The rabbit was fixed on the rabbit holder. Before surgery, the right lower limb hair was shaved, and the femoral condyle was palpated to locate the gastrocnemius attachment point and then marked with a surgical pen. After disinfection of the surgical area with iodophor, the surgeon held the ankle joint in the left hand to maintain the ankle joint bent at 90 degrees while pulling it back to extend the knee joint to the maximum, placing the left thumb on the gastrocnemius near the Achilles tendon, and holding the scalpel in the right hand to enter the skin at the marked point (Figure 1). The blade was placed perpendicular to the direction of the muscle fiber and used to incise at the place where the gastrocnemius attaches to the femoral condyle, then sliding the handle 2 mm outward simultaneously. The surgeon's left thumb was used to palpate the vibration when the gastrocnemius was cut. The gastrocnemius was damaged but not completely sectioned. Then, the surgeon removed the scalpel and obtained hemostasis using a cotton ball for 1 minute. The surgical procedures were performed by the same surgeon with extensive clinical experience and more than 3 years of acupotomology experience.

2.3. Medical Imaging Evaluation. Before sampling, we obtained anteroposterior and lateral view X-ray films of six lower limbs in each group to observe the changes in tibiofemoral joint space and osteophytes. X-ray detection parameters were as follows: peak 50 kV, irradiation current 200 mA, irradiation time 5 ms, and irradiation height 120 cm. All anteroposterior radiographs were graded according to the Kellgren and Lawrence (K-L) scores [20]. The image of the X-ray was observed and evaluated blindly by two investigators. The mean value of the score was considered for statistical purposes.

To observe the changes of subchondral bone and bone trabeculae in more detail, the right femoral and tibial ends of three rabbits in the LGI group and one in the control group at 8 weeks were scanned using microcomputed tomography (Quantum GX PE micro-CT imaging system, 9 kV, 60 uA, FOV 36 mm) after sampling. We captured the sagittal images of the centre of the medial and lateral condyles of the femoral end of the knee joint to observe the changes at the most loaded position of the articular condyle. The micro-CT images were evaluated and analyzed by 2 experienced orthopedic surgeons.

2.4. Gastrocnemius Muscle Observation. The gross morphology of the gastrocnemius of six rabbits in each group was measured, and the MG and LG were separated to measure

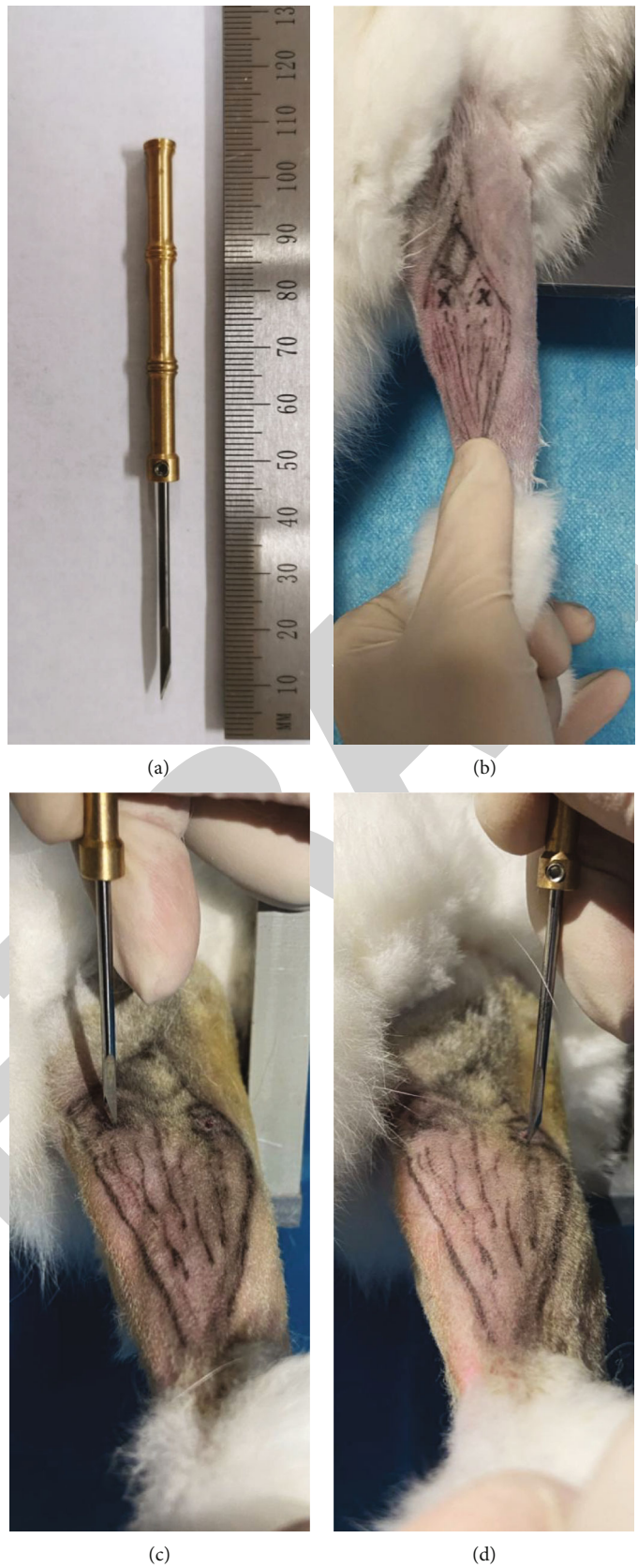

Figure 1: (a) The scalpel. (b) The popliteal fossa, posterior thigh muscles, and gastrocnemius; the cross marks the entry point of the scalpel. (c, d) The blade direction of the scalpel.

the respective wet weights using an electronic balance (BT223S; Beijing Sartorius Instrument System, China). The two ends of the MG and LG were fixed on cardboard with pins and fixed with 4% paraformaldehyde. The parts in the belly of the muscles were embedded in paraffin and then cut into 4 μm sections and stained with hematoxylin and eosin (HE Staining Kit, G1120, Solarbio) to observe the muscle fiber morphology. In each section, we randomly selected five fields using a 40× objective. Image-Pro Plus 6.0 (IPP 6.0) was used to compare the average diameter of muscle fibers.

2.5. Histology. The right distal femur was harvested at each group ($n = 6$ knees/interval), fixed with 4% paraformaldehyde, decalcified with EDTA decalcifying solution (pH 7.2, E1171, Solarbio), and paraffin-embedded after conventional dehydration. The sections were created along the sagittal plane (6 μm), and we observed the femoral condyle cartilage and subchondral bone morphology. Safranin O fast green (Modified Safranin O Fast Green FCF Cartilage Stain Kit, G1371, Solarbio) was used to observe the morphological changes of the femoral condyle cartilage and subchondral bone. The Mankin score was used to evaluate articular cartilage changes [21]. Masson's Trichrome Stain (G1340, Solarbio) was used to evaluate cartilage collagen changes and calculate the collagen volume fraction (CVF). Representative sections of the tibiofemoral articular surface were photographed after observation under the microscope (Olympus BX43F Microscope), and the areas of interest were evaluated using IPP 6.0. The scores were calculated blindly by two researchers and averaged for statistical comparison.

2.6. Immunohistochemistry. The sections were dried at 65°C for 1 hour. We used xylene and gradient alcohol dewaxing to water and washed twice with phosphate-buffered saline for 5 minutes. Antigen repair was performed with sodium citrate buffer in a 98°C water bath. An endogenous enzyme blocker was placed for 10 minutes. Primary antibody against Col-II (Proteintech Cat# 28459-1-AP, RRID:AB_2881147), MMP 13 (Proteintech Cat# 18165-1-AP, RRID:AB_2144858), and ITG-β1 (Bioss Cat# bs-0486R, RRID:AB_10856339) was incubated overnight at 4°C, and phosphate-buffered saline was used instead of primary antibody in the negative control. DAB (DAB Substrate kit, 20×, DA1010, Solarbio) was used for 7 minutes as a chromogenic reagent after applying the secondary antibody (ZSGB-Bio Cat# PV-6001, RRID: AB_2864333) at 37°C for 30 minutes. Tissue sections were observed using a 20× objective lens, and we photographed representatives region of the tibiofemoral articular surface while the background light source was consistent. IPP 6.0 was used to analyze the average optical density (AOD) of the images. Statistics were obtained using the mean value of the two researchers' calculations.

2.7. Statistical Analysis. All measurement data were expressed as mean ± standard deviation. SPSS 20.0 statistical software was used to analyze the data. The Shapiro-Wilk test was used to assess normality, and the Levene test evaluated homogeneity of variance. Muscle wet weight and muscle fiber diameter were calculated using the independent sample T-test, the T-test of paired samples, and the two-sample nonparametric test. The K-L scores, Mankin scores, CVF, and AOD of the immunohistochemical samples were compared using the least significant difference test, and the Kruskal-Wallis test was used to compare nonparametric values among several groups. Differences were considered statistically significant when $p < 0.05$. Figures were generated using GraphPad Prism 9.0.

3. Results

3.1. X-Ray. In the 6- and 8-week groups, X-rays of the MGI group showed suspected narrowing of tibiofemoral joint space, suspected osteophytes, or evident osteophyte formation (Figure 2(a)). In the 6-week control group, X-ray findings of the tibiofemoral joint were normal. However, in the 8-week control group, some rabbits showed normal knee radiographs, while others showed suspicious narrowing of joint space and suspicious osteophytes. The K-L scores showed significant differences between the 6-week MGI and LGI groups (MGI group: 1.08 ± 0.2, $p = 0.008$; LGI group: 1.17 ± 0.26, $p = 0.003$) and the control group (0.08 ± 0.2). However, in the 8-week group, only the LGI group (1.67 ± 0.41) showed significantly higher ratings than the control group (0.42 ± 0.49) ($p = 0.003$) (Figure 2(b)).

3.2. Micro-CT Measurements of Bone. The micro-CT images of the femoral condyle and tibia in the LGI group showed increased subchondral bone density, slightly disordered trabeculae, a rough and unrounded cartilage surface, and thickening of the high-density areas on the bone surface. The knee joint of the normal rabbit at 8 weeks was characterized by a uniform and regular arrangement of bone trabeculae with moderate spacing and radial distribution along the direction of the force. There was no significant difference in the images of the medial and lateral condyles (Figure 3).

3.3. Gastrocnemius Change. The gastrocnemius was observed close to the plantaris and soleus muscles, and the plantaris was substantial (Figure 4(a)). The wet weight of the gastrocnemius was measured. The MG of normal rabbits (6 weeks 3.8 ± 0.46, 8 weeks 3.82 ± 0.38) were significantly lighter than the LG (6 weeks 6.39 ± 0.94, 8 weeks 6.16 ± 0.59) at 6 and 8 weeks ($p < 0.001$) (Figure 4(b)). The corresponding side of the gastrocnemius at 6 and 8 weeks showed no differences. At weeks 6 and 8, there were no differences in wet muscle weight of the injured head of gastrocnemius in the MGI and LGI groups and the blank control group. However, comparing the left and right leg muscle wet weights in each group, we found that the wet weight of the LG was significantly different in the LGI group only at 8 weeks; the injured side weight (right 6.4 ± 0.82) was heavier than that on the uninjured side (left 6.02 ± 0.94) ($p = 0.13$) (Figure 4(c)).

HE staining showed that muscle fibers in the injured group became round and blunt, the nuclei were increased or even broken, and collagen hyperplasia was seen in the space between muscle fibers. The muscle fibers in the normal group were polygonal, and the nuclei were located at the edge of muscle fibers (Figure 4(d)). In the control group,

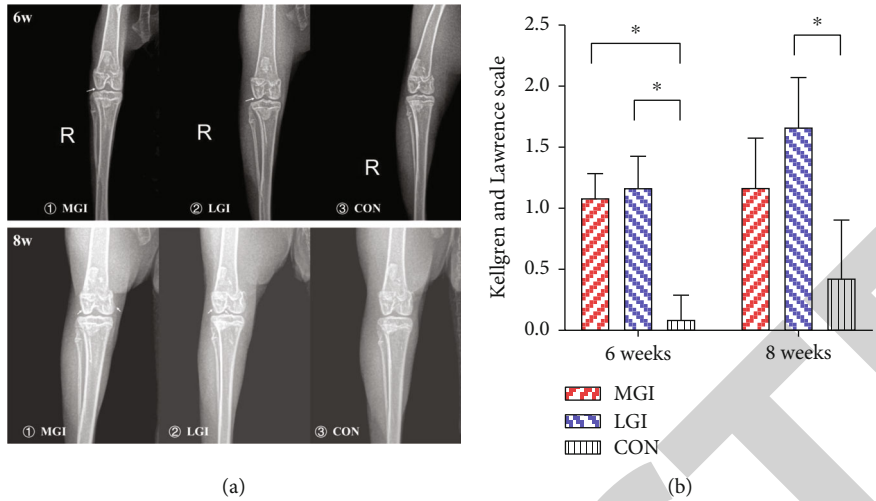

(a) (b)

Figure 2: (a) X-ray of the right leg of each group at each interval. The arrow points to the suspected osteophyte. (b) K-L scores, $^{*}p < 0.05$.

there was no significant difference in the mean diameter of muscle fibers between the MG (44.65 ± 2.64) and LG (44.81 ± 4.18) at 6 weeks; however, the difference was significant at 8 weeks (MG 52.36 ± 3.3, LG 56.18 ± 2.54) ($p = 0.002$), and the mean diameter of MG and LG of the 8-week group was significantly larger than that of the 6-week group (MG $p = 0.001$, LG $p < 0.001$). The comparison of the mean diameter of muscle fibers between the injured side of the gastrocnemius and the corresponding side of the control group showed that the MGI (6 weeks 37.08 ± 4.25, 8 weeks 36.16 ± 4.78) and LGI groups (6 weeks 39.5 ± 2.79, 8 weeks 41.3 ± 3.49) were lower than that on the control group at 6 and 8 weeks. All mean diameters of injured muscle fibers were lower than that of normal muscle. There was no significant difference in the mean diameter between 6 and 8 weeks of injured gastrocnemius (Figure 4(e)).

3.4. Collagen Change. Safranin O fast green staining showed no severe damage of the cartilage layer in the injured group, while the cartilage showed varying degrees of matrix discoloration, cell cluster or cell decrease, and reproduction or disappearance of tide lines (Figure 5(a)). The Mankin scores were significantly higher in the injured group than in the control group at 6 and 8 weeks ($p < 0.05$) (Figure 5(b)). Masson staining of the sections showed partial discoloration and uneven tide lines as well as clumps of cells (Figure 5(c)). Six weeks after gastrocnemius injury, the CVF of the right femoral condyle was lower only in the MGI group than in the blank group ($p < 0.001$). The CVF of the MGI ($p = 0.004$) and LGI groups ($p = 0.009$) were significantly lower than the control group at 8 weeks (Figure 5(d)).

3.5. Immunohistochemistry. Immunohistochemical staining for Col-II showed no significant difference between the injured and the control groups at 6 weeks. The AOD at 8 weeks indicates that the Col-II content in the injured group (MGI, $p = 0.002$; LGI, $p = 0.039$) was significantly lower than the control group's (Figures 6(a) and 6(b)). Immunohistochemical results of the AOD of MMP13 in the MGI and LGI groups were significantly higher than in the control group at 6 (MGI, $p = 0.004$; LGI, $p = 0.028$) and 8 weeks (MGI, $p = 0.011$; LGI, $p = 0.011$) (Figures 6(c) and 6(d)). The immunohistochemical results the AOD of ITG-β1 in the LGI group ($p = 0.015$) was significantly higher than in the control group at 6 weeks, while the injured group (MGI, $p = 0.019$; LGI, $p < 0.001$) was higher than the control group at 8 weeks. Meanwhile, the AOD of ITG-β1 in the LGI group was always higher than that in the MGI group (6 weeks: $p = 0.012$; 8 weeks: $p = 0.005$).

4. Discussion

When selecting a modeling method, we considered various animal models of muscle injury. There are three major types of muscle damage, including contusion, strain, and laceration. Laceration models are more consistent and reproducible and commonly evaluate posttraumatic scars [22]. Furthermore, many laceration models require a specific depth and width of incision at the musculature by opening the skin [23–25]. Because gastrocnemius palpation can reveal atrophy, spasm, and tension in several forms, and the palpation position was the attachment of the femoral condyle of the MG and LG, the experimental design required an abnormal state of the attachment site of the femoral condyle of the gastrocnemius. However, there is no strict agreement regarding the degree of damage. We ultimately chose the method of semidetaching the MG and LG insertion point and maintaining the cutting position and degree same to the greatest extent possible, while extensive skin incision was not performed to reduce skin tension damage. The rabbit can perform daily running and living activities as long as the gastrocnemius is not entirely severed. Such modeling is more closely related to real-life patient performance. Our modeling method is convenient and straightforward in terms of time and operation; however, it can only ensure the relative consistency of the model. Due to the differences in muscle structure and function of the MG and LG, humans are often more vulnerable to injuries of the MG [26, 27]. We

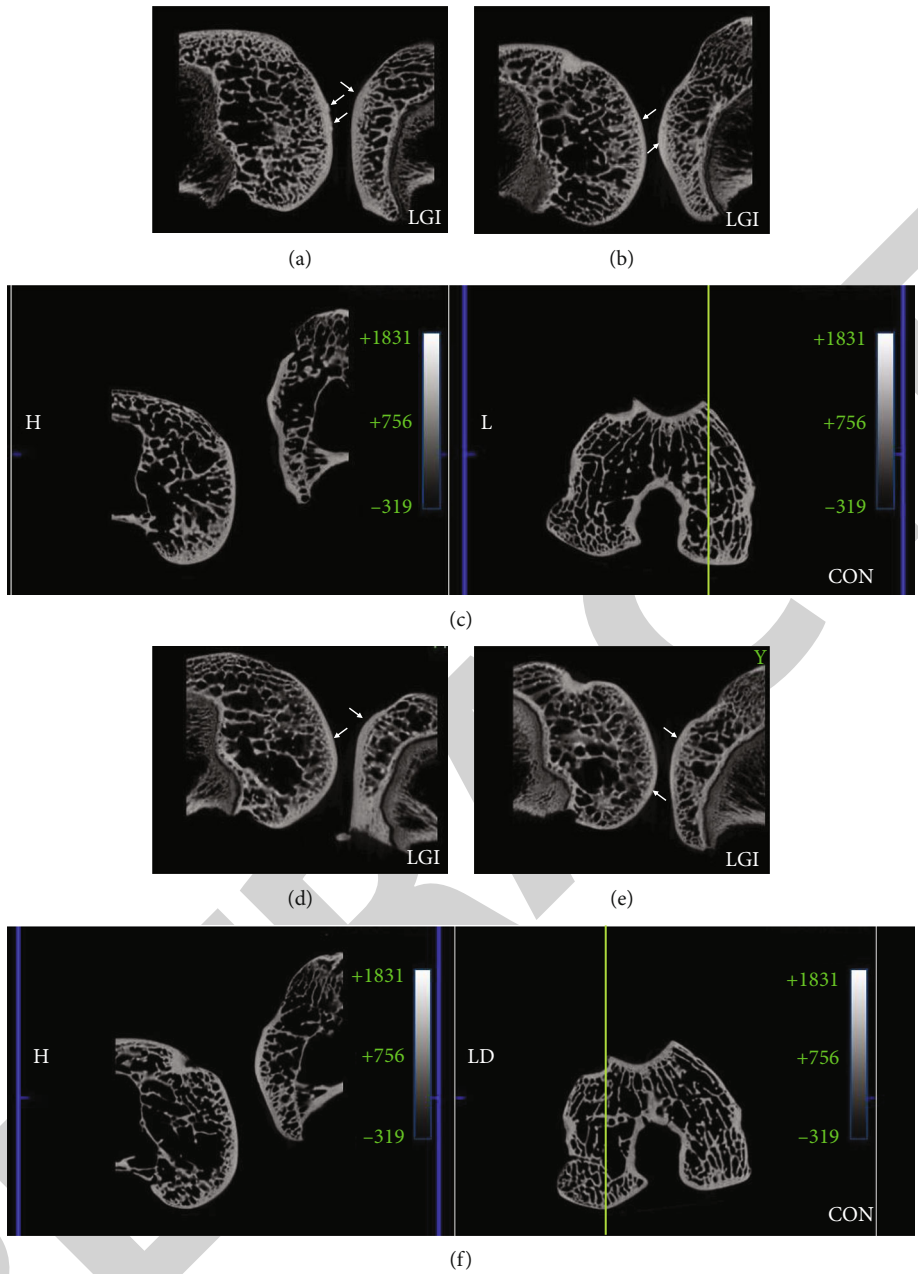

Figure 3: Micro-CT of the LGI and control groups. (a–c) The medial condyle of the right leg. (d–f) The external condyle. The green line position in (c) and (f) marks the sagittal observation position of the control group. The LGI group showed the same position. The arrow indicates the rough surface of the bone.

wanted to distinguish the differences in the pathological changes of the femoral condyle caused by injury of the MG and LG at the beginning of the study. We observed that the wet weight of the MG in the normal group was significantly lower than that of the LG at 6 and 8 weeks, while the mean muscle fiber diameter of the MG was significantly smaller than that of the LG at 8 weeks. This finding suggests differences between the MG and LG muscles in rabbits, and the differences in muscle fiber diameter may be related to the development time of rabbits. From the experimental results, we could only observe that the wet weight of the injured muscle head showed a tendency to be lighter than the healthy side at 6 weeks. The MG showed a tendency to be lighter than the healthy side at 8 weeks, while the LG showed a significant wet weight gain. The average diameter of muscle fibers in the injured muscle head was significantly smaller than that of the control group, except for the LGI group at 6 weeks, which also showed a decreasing trend. Although the observed reduction in gastrocnemius diameter is consistent with muscle atrophy, wet muscle weight did not show a completely downward trend. We can only confirm that the model caused the gastrocnemius to atrophy and produce fibrous hyperplasia and scarring.

We did not observe significant differences in the femoral condyle caused by MG and LG injury. This finding may be related to compensation for gastrocnemius injury by other

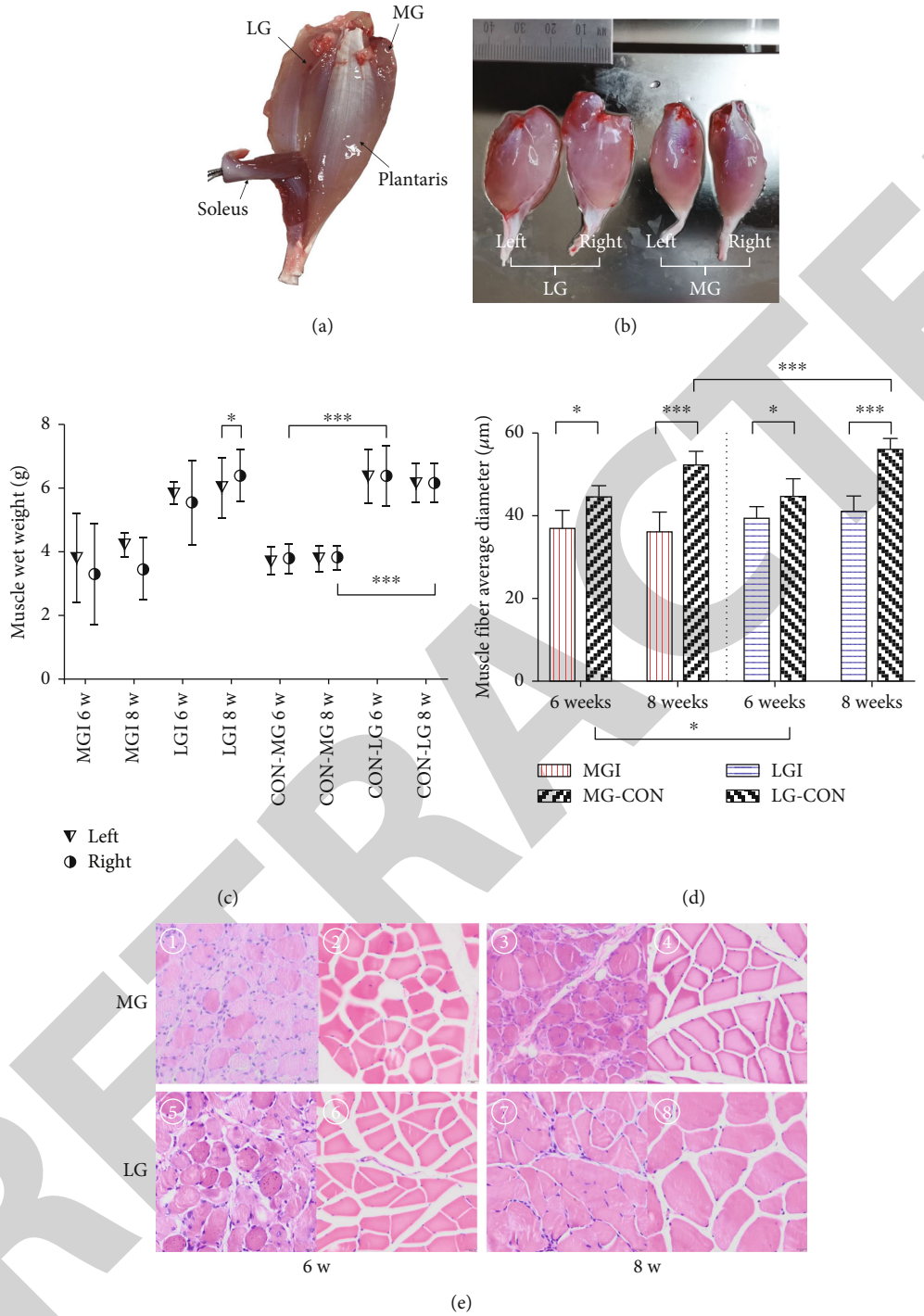

FIGURE 4: (a) General view of the abdominal flank of the gastrocnemius. The soleus and plantaris are next to the MG and LG. (b) Comparison of MG and LG. (c) Quantitative analysis of the wet weight of gastrocnemius. The findings distinguish MG and LG and interval, $^{***}p < 0.001$. (d) HE staining of the gastrocnemius at 40x magnification. ①③⑤⑦ The injured group show inflammation and muscle fiber atrophy; ②④⑥⑧ control group. (e) Quantitative analysis of the mean diameter of muscle fiber and the value represents the mean value of each group.

calf muscles closely attached to the gastrocnemius such as soleus and plantaris. In particular, the plantaris appeared as a robust and developed muscle in the rabbit calf and is closely attached to the MG, while the plantaris is a small fusiform muscle or even absent in humans [28]. Squatting is the primary posture of rabbits, and the change of femoral condyle may be affected by the behavioral habits of rabbits after gastrocnemius injury. At 8 weeks, it was evident that the MGI and LGI groups showed significant pathological features in the femoral condylar cartilage. At 6 weeks, we observed more of a transitional stage in the pathological process. The MGI group showed more significant differences in

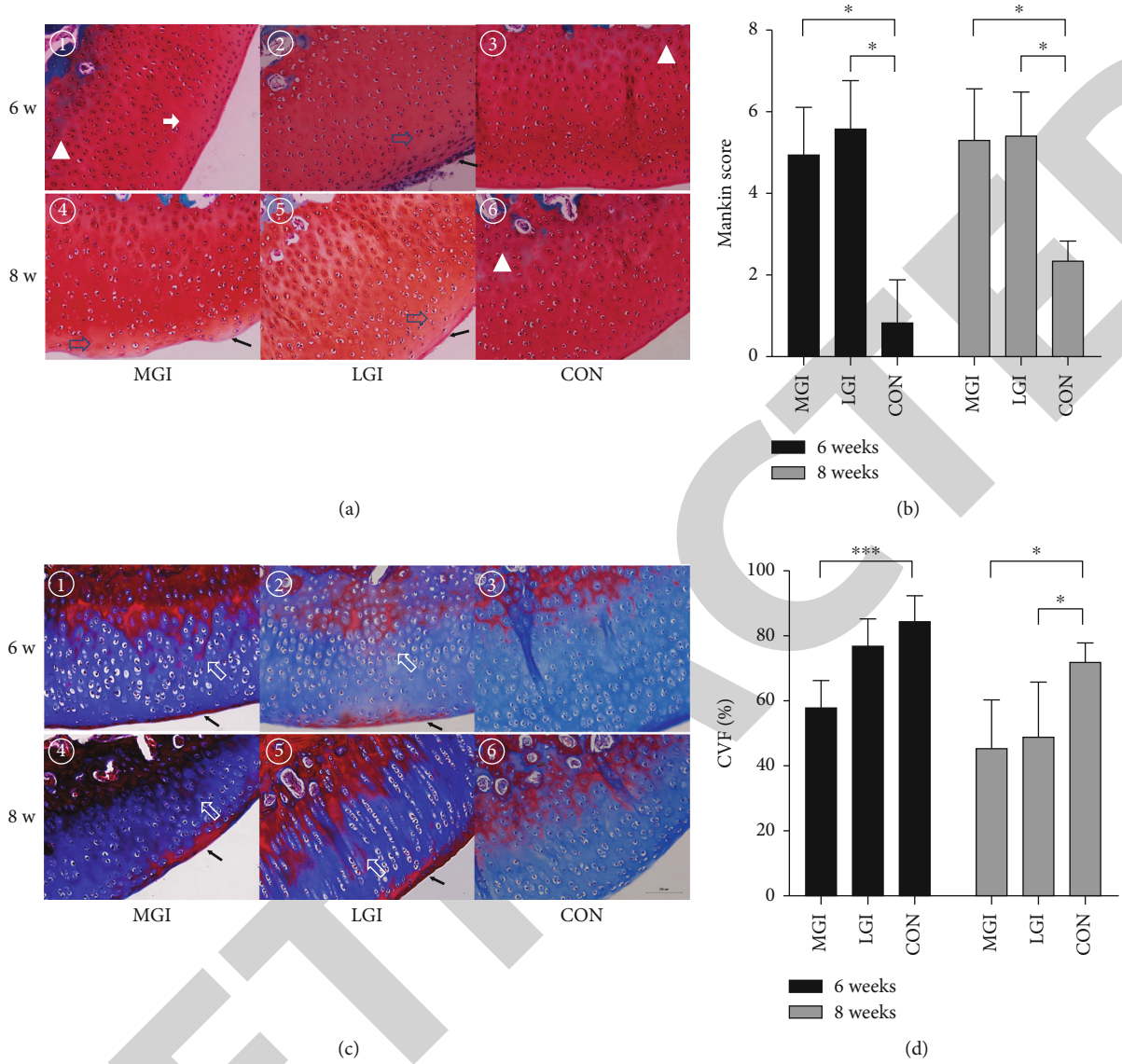

Figure 5: (a) Safranin O fast green staining. The black arrow points to the uneven surface of the cartilage, the white arrow points to the site of cell reduction, the blue hollow arrow points to the faded region, and "▲" marks the position of the tide line. (b) Mankin scores reveal degeneration of cartilage in the injured group. (c) Masson stain: the area where the white hollow arrow points to shows tidal intrusion into the cartilage layer, and the black arrow points to the site of collagen damage in the upper cartilage. (d) Semiquantitative analysis of the CVF (%).

the femoral condyle at 6 weeks, suggesting that the MG is more sensitive to injury and develops pathological changes of the femoral condyle more quickly. The K-L scores distinguished the injured and the control groups; however, the injured group did not achieve severe arthritis. This finding may be explained by the fact that the animal is in an early stage of knee degeneration without evident osseous changes. Due to financial constraints, we only chose to compare the tibiofemoral joints with LG injury at 8 weeks with normal rabbits using micro-CT. The results showed that the surfaces of the femur and tibia of the knee in the LGI group were rough and uneven, and the high-signal areas were thicker. After gastrocnemius injury, the compensatory densities of the subchondral bone and the femoral and tibial end of the knee joint were likely related to cartilage injuries. We obtained gross views of the femoral condyle and observed no apparent articular surface injury. The injury to femoral segment cartilage was confirmed by comparing the Mankin score, CVF, and AOD. The Mankin score showed significant pathological changes in the cartilage of the injured group at each interval, which also suggests a state of early degeneration. The CVF results calculated using Masson staining showed that collagen status was consistent with the trend of the immunohistochemical results in Col-II. These findings suggest a reduction of collagen in the femoral condyle cartilage of the tibiofemoral joint and cartilage degeneration. Immunohistochemical results showed that MMP13 expression appeared at weeks 6 and 8, while Col-II showed only a decreasing tendency at 6 weeks and significantly decreased only at 8 weeks. This finding suggests that the expression of

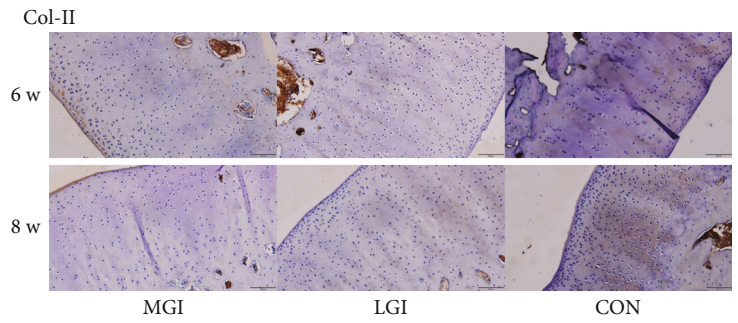

(a)

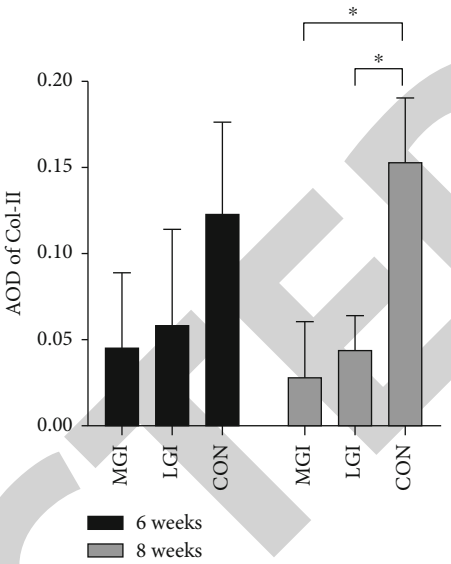

(b)

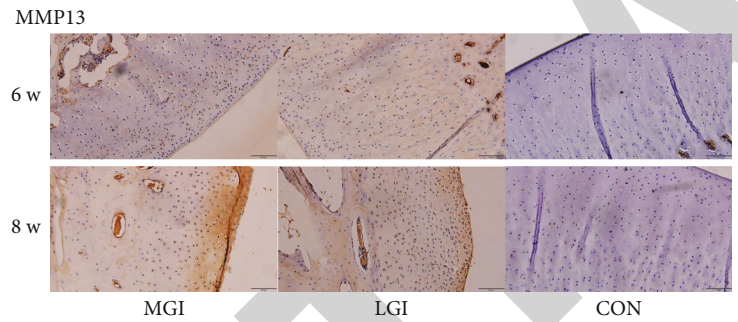

(c)

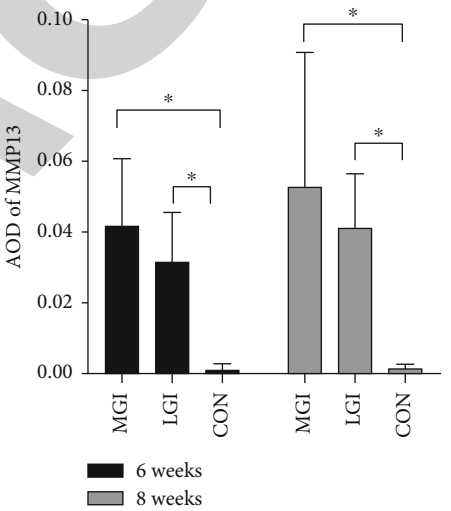

(d)

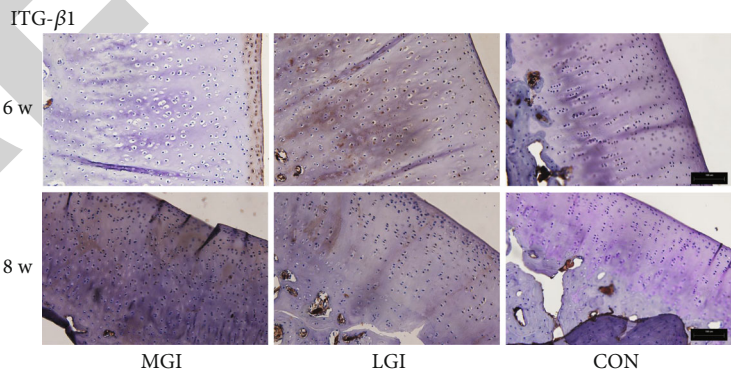

(e)

Figure 6: Continued.

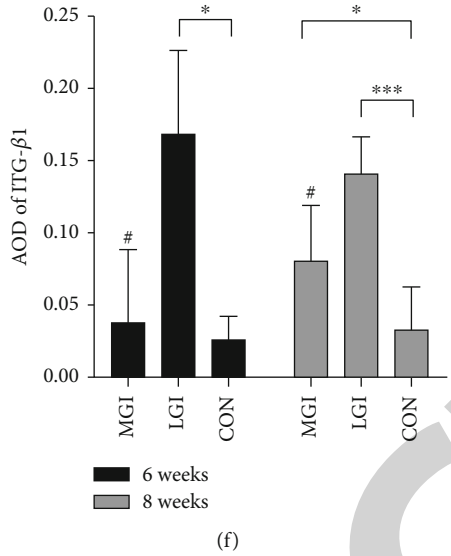

Figure 6: (a) Immunohistochemistry for Col-II revealing that the amount of collagen in the injured group was less than that of the group. (b) Semiquantitative analysis of the AOD of Col-II. (c) Immunohistochemistry reveals that the injured group's cartilage layer began to express MMP13, while there was almost no expression in the control group. (d) Semiquantitative analysis of the AOD of MMP13. (e) Immunohistochemistry showed that ITG-β1 increased significantly in the 6-week MGI group and the LGI group. (f) Semiquantitative analysis of the AOD of ITG-β1 ($^{\#}$the MGI group versus the LGI group, $p < 0.05$).

MMP13 in collagen decomposition occurs first, while the process of Col-II decomposition is significantly reduced later under its influence. Further experiments are needed to verify the specific pathway. Safranin O fast green staining showed that substrate fading might be related to aggrecan reduction, a finding that we will study in the future. Another observation was that ITG-β1 was consistently higher in the LGI group than in the control group. The level of ITG-β1 in the MGI group was not significantly increased at 6 weeks and was significantly higher than that in the control group at 8 weeks, but it was not at the same level as that in the LGI group. It has been proved that ITG-β1 is elevated in arthritic chondrocytes and is related to the degree of injury [29, 30]. The results of this study suggest that ITG-β1 may be upregulated by mechanical changes after gastrocnemius injury. There are some differences in the changes of mechanical factor ITG-β1 caused by MG and LG injury, which may be related to differences in the progression of KOA. More specific studies are still needed to study the mechanical changes and conduction of the knee joint induced by gastrocnemius injury.

Gastrocnemius injury can cause pathological changes in the femoral condyle of the tibiofemoral joint, suggesting ideas and an experimental basis for the early prevention and treatment of KOA. Attention should be paid to the effect of gastrocnemius in KOA in addition to the quadriceps and hamstring muscles [31, 32]. The progression of KOA is a long-term process, and the results at different time points after modeling suggested pathological progression, which may be severe. This finding also suggests that KOA should be prevented and treated early; attention should be paid to gastrocnemius relaxation and softening. We could not elucidate the specific biomechanical changes and access mechanism of knee joints caused by gastrocnemius injury and failed to observe differences in knee injury caused by MG and LG. For this reason, we will strive to develop mechanistic experiments to help develop treatment measures.

5. Conclusions

Atrophy, fibrosis, and scarring occurred 8 weeks after gastrocnemius injury in rabbit, possibly affecting the biomechanical properties of the muscle and affecting stress at the tibiofemoral joint. The tibiofemoral joint presents with mechanical imbalance, and the femoral condyle develops pathological changes. The specific manifestations are coarse articular surfaces, suspicious narrowing of articular space, and development of osteophytes. The pathological morphological changes in femoral condyle cartilage and the decrease of Col-II may be caused by abnormally increased expression of MMP13 that can lead to early knee osteoarthritis. And this mechanism may be related to the regulation of mechanical sensitive factor ITG-β1 in the cartilage. This study provides a concept that may lead to early prevention and treatment of tibiofemoral arthritis.

Data Availability

The datasets analyzed during the current study are available from the corresponding author upon reasonable request.

Ethical Approval

Experiments were performed under a project license (Ethics Reference No. BUCM–4–2020112003-4070) granted by the Animal Ethics Committee at Beijing University of Chinese

Medicine approved the animal experiments and complied with the guidelines of the ARRIVE Guidelines and the Use and Care of laboratory animals published by US National Institutes of Health. We did our best to decrease the number of rabbits and suffering during the study.

Conflicts of Interest

The authors declare no conflict of interest.

Authors' Contributions

Conceptualization was done by R.W. and Y.L. Methodology was done by J.S., Y.L., Y.H., and Y.C. Validation was done by J.S., Y.H., and J.W. Formal analysis was performed by Y.H., Y.C., J.W., and R.W. Investigation was performed by X.Z. and R.W. Resources were acquired by Y.L., J.S., Y.H., and J.W. Data curation was performed by Y.H., Y.C., and X.Z.. Writing—original draft preparation was done by Y.L. Visualization was done by Y.L., J.S., and Y.H. Funding was acquired by R.W. All authors have read and agreed to the published version of the manuscript.

Acknowledgments

We thank Junfeng Gao (Dongfang Hospital of Beijing University of Chinese Medicine) for guidance in micro-CT photography and Xueling Kang (School of Acupuncture-Moxibustion and Tuina, Beijing University of Chinese Medicine) for her help in making paraffin sections. This work was supported by grants from the Fundamental Research Funds for the Central Universities (2020–JYB–ZDGG–064) and the Research and Development Fund of Beijing University of Chinese Medicine (2019–ZXFJJ–120).

Supplementary Materials

The Kellgren and Lawrence grading system is shown in the supplementary materials. *(Supplementary Materials)*

References

[1] D. J. Hunter and S. Bierma-Zeinstra, "Osteoarthritis," *The Lancet*, vol. 393, no. 10182, pp. 1745–1759, 2019.

[2] M. J. Lespasio, N. S. Piuzzi, M. E. Husni, G. F. Muschler, A. Guarino, and M. A. Mont, "Knee osteoarthritis: a primer," *The Permanente Journal*, vol. 21, pp. 16–183, 2017.

[3] S. L. Kolasinski, T. Neogi, M. C. Hochberg et al., "2019 American College of Rheumatology/Arthritis Foundation guideline for the management of osteoarthritis of the hand, hip, and knee," *Arthritis & Rheumatology*, vol. 72, no. 2, pp. 149–162, 2020.

[4] T. Georgiev and A. K. Angelov, "Modifiable risk factors in knee osteoarthritis: treatment implications," *Rheumatology International*, vol. 39, no. 7, pp. 1145–1157, 2019.

[5] J. E. Cunha, G. M. Barbosa, P. Castro et al., "Knee osteoarthritis induces atrophy and neuromuscular junction remodeling in the quadriceps and tibialis anterior muscles of rats," *Scientific Reports*, vol. 9, no. 1, p. 6366, 2019.

[6] C. Bartholdy, C. Juhl, R. Christensen, H. Lund, W. Zhang, and M. Henriksen, "The role of muscle strengthening in exercise therapy for knee osteoarthritis: a systematic review and meta-regression analysis of randomized trials," *Seminars in Arthritis and Rheumatism*, vol. 47, no. 1, pp. 9–21, 2017.

[7] J. F. Sisante, N. Wang, D. T. Felson et al., "Influence of antagonistic hamstring coactivation on measurement of quadriceps strength in older adults," *PM & R : The Journal of Injury, Function, and Rehabilitation*, vol. 12, no. 5, pp. 470–478, 2020.

[8] S. Blair, M. J. Lake, R. Ding, and T. Sterzing, "Magnitude and variability of gait characteristics when walking on an irregular surface at different speeds," *Human Movement Science*, vol. 59, pp. 112–120, 2018.

[9] M. Cibulka, A. Wenthe, Z. Boyle et al., "Variation in medial and lateral gastrocnemius muscle activity with foot position," *International Journal of Sports Physical Therapy*, vol. 12, no. 2, pp. 233–241, 2017.

[10] J. A. Friederich and R. A. Brand, "Muscle fiber architecture in the human lower limb," *Journal of Biomechanics*, vol. 23, no. 1, pp. 91–95, 1990.

[11] F. Li, C. Weng, N. Wang et al., "The passive range of motion of ankle dorsiflexion and features of surface electromyographic signals of gastrocnemius and tibialis anterior in patients with medial knee displacement," *Chinese Journal of Sports Medicine*, vol. 36, pp. 14–16, 2017.

[12] R. Kitatani, K. Ohata, S. Sato et al., "Ankle muscle coactivation and its relationship with ankle joint kinematics and kinetics during gait in hemiplegic patients after stroke," *Somatosensory & Motor Research*, vol. 33, no. 2, pp. 79–85, 2016.

[13] J. B. Morrison, "The mechanics of the knee joint in relation to normal walking," *Journal of Biomechanics*, vol. 3, no. 1, pp. 51–61, 1970.

[14] M. J. Booij, R. Richards, J. Harlaar, and J. C. van den Noort, "Effect of walking with a modified gait on activation patterns of the knee spanning muscles in people with medial knee osteoarthritis," *The Knee*, vol. 27, no. 1, pp. 198–206, 2020.

[15] D. R. Armfield, D. H. Kim, J. D. Towers, J. P. Bradley, and D. D. Robertson, "Sports-related muscle injury in the lower extremity," *Clinics in Sports Medicine*, vol. 25, no. 4, pp. 803–842, 2006.

[16] D. Eyre, "Collagen of articular cartilage," *Arthritis Research*, vol. 4, no. 1, pp. 30–35, 2002.

[17] D. Heinegard, "Fell-Muir lecture: proteoglycans and more – from molecules to biology," *International Journal of Experimental Pathology*, vol. 90, no. 6, pp. 575–586, 2009.

[18] H. Li, D. Wang, Y. Yuan, and J. Min, "New insights on the MMP-13 regulatory network in the pathogenesis of early osteoarthritis," *Arthritis Research & Therapy*, vol. 19, no. 1, p. 248, 2017.

[19] L. Cueru, C. Bougault, A. Aszodi, Y. Berthier, F. Mallein-Gerin, and A. M. Sfarghiu, "Mechanical and physicochemical responses for hyaline cartilage: role of protein β1 integrin in mechanotransduction," *Computer Methods in Biomechanics and Biomedical Engineering*, vol. 16, no. sup1, pp. 330-331, 2013.

[20] J. H. Kellgren and J. S. Lawrence, "Radiological assessment of osteo-arthrosis," *Annals of the Rheumatic Diseases*, vol. 16, no. 4, pp. 494–502, 1957.

[21] H. J. Mankin and L. Lippiello, "Biochemical and metabolic abnormalities in articular cartilage from osteo-arthritic human hips," *The Journal of Bone and Joint Surgery. American Volume*, vol. 52, no. 3, pp. 424–434, 1970.